



Norwegian University
of Life Sciences

Master's Thesis 2019 30 ECTS

Faculty of Science and Technology

Hyperspectral imaging as a tool to study solar induced photoluminescence from PV modules

Ingeborg Eriksdatter Høiaas
Environmental Physics and Renewable Energy

Abstract

The installed solar photovoltaic (PV) capacity in the world is increasing and solar PV is becoming a bigger part of the energy mix. Reviewed literature on PV field performance show an average degradation rate of 0.8%/year, with the median at 0.5%/year (Jordan & Kurtz, 2012) [1]. This information, in addition to the forecasted increase in PV capacity, means it is exceedingly important to understand the long-term degradation of installed modules, both to predict when modules need to be replaced and to reduce the effects of degradation at an early stage. A contactless method, which has proven to be promising in detecting crystal imperfections like grain boundaries, line defects and point defects, is hyperspectral photoluminescence (PL) imaging in the Short-Wave InfraRed (SWIR) wavelength region (1000 nm - 2500 nm). This technique makes it possible to map mechanisms for recombination of photogenerated charge carriers in semiconductors, based on the energy level of the emitted signal. To use this technique for field inspection the weak luminescence signal must be separated from the much stronger ambient sunlight. We have explored a method for doing this by calibrating images with a white reference and subtracting a short circuit signal from an open circuit signal.

We present the experimental data and hypothesis we have gathered with respect to methodology and signal recordings conducted with hyperspectral cameras of PV modules illuminated with the solar spectrum. Preliminary results using irradiation from a solar simulator and laser in a laboratory environment show that there is a strong signal in the band-to-band (BB) wavelength area, both from a mc-Si solar cell, and a commercial mc-Si module. However, the signal recordings from outdoor data collections have a significantly lower signal to noise ratio than the laboratory results.

By comparing cell regions with non-cell regions, and comparing signals from different operating conditions we have gathered results that promote this as a promising technique. Nonetheless, it needs to be further improved to provide the information needed to evaluate material performance of solar cells.

Sammendrag

Den installerte fotovoltaiske (PV) kraftproduksjonen i verden øker og solceller har blitt en stor del av energimiksen. En litteraturundersøkelse på solcellers ytelse i felt viser en degraderingsrate på 0.8 %/år, med en median på 0.5%/år (Jordan Kurtz, 2012). Ved å sette denne informasjonen i sammenheng med prognosene for installerte solceller i verden ser man et tydelig behov for å forstå den langsigtige degraderingen i installerte PV moduler. Både for å predikere når en modul må byttes ut, og for å redusere effekten av degradering på et tidlig tidspunkt. En kontaktløs metode, som har vist seg å være lovende for å detektere defekter som korngrenser, linje defekter og punkt defekter er hyperspektral fotoluminescens (PL) avbildning i kortbølget infrarødt (SWIR) bølgelengde området (1000 nm - 2500 nm). Denne tilnærmingen gjør det mulig å kartlegge rekombinasjonsmekanismer basert på energinivået til det emitterte signalet.

I denne oppgaven blir våre funn av hvordan hyperspektral PL avbildning kan bli brukt til å inspirere degradering av utendørs PV moduler presentert, og hvordan teknikken kan brukes til å effektivt undersøke og overvåke moduler i drift. Luminescens signalet som blir emittert fra solcellematerialet er utfordrende å detektere korrekt fra utendørs paneler på grunn av reflektert sollys og absorbert signal i vanndamp. Vi vil her presentere de eksperimentelle dataene og hypotesene, fra hyperspektral avbildning av solceller belyst med solspekteret, med hensyn til metodologi og innhentet signal. Preliminære resultater fra belysning med en solsimulator og laser i laboratoriet viser at det er sterke signaler i bånd-til-bånd (BB) bølgelengdeområdet (\approx 1120 nm) fra en enkelt mc-Si solcelle og fra en kommersiell mc-Si modul. Signalene som ble avbildet utendørs har en mye lavere signal-til-støy rate, noe som gjør det vanskelig å si om det er et PL signal vi ser. Ved å sammenligne signalet fra celleområder med signaler fra en hvitreferanse og et hvitt område under modulglasset ser man at signalet fra områder fra celler har et mye høyere signal i BB-området enn signal fra ikke-celle områder.

Våre resultater tyder på dette er en lovende teknikk, men for at den skal kunne brukes til å analysere materialkvalitet og degradering må den forbedres ytterligere.

Preface and acknowledgements

The present work is a Master thesis in the Master of Science program in Environmental Physics and Renewable energy with specialization in Experimental Methods and Image Analysis at the Norwegian University of Life Sciences (NMBU). The thesis has been part of the work done by the Solar Energy group at the department of Science and Technology led by Professor Espen Olsen. The group is making efforts to characterize materials by hyperspectral imaging and this project is part of the groups goal to use hyperspectral photoluminescence imaging as a tool to study degradation of photovoltaic modules outdoor. The work was carried out in the NMBU Hyperspectral Imaging Lab, outside and on top of the faculty building, from January to May 2019.

First of all, I would like to thank my supervisor Associate Professor Ingunn Burud for getting me involved in this exciting project, and for giving me valuable feedback throughout the semester.

I would also like to thank my co-supervisor Espen Olsen who have welcomed any questions I might have had, as well as providing constructive discussions of the results. Thank you Andreas Flø for showing me how to use the hyperspectral instruments outdoor, and whom have been extremely helpful in regard to practical solutions in the experimental design. Thank you Torbjørn Mehl for being close at hand during the laboratory work, and for giving constructive inputs on the quality of the results. I also want to thank Tom Ringstad for soldering solar cells with a steady hand, and for lending me screwdrivers and multimeters when needed.

Last but not least I would like to thank Marija Vuković, whom have patiently shared her preliminary work and knowledge of hyperspectral imaging, and whom I have collaborated with closely throughout the project.

Ingeborg Høiaas
NMBU, Ås
May 28, 2019

List of abbreviations

- BB** Band to Band
CCD Charge-Couple Device
DRL Defect Related Luminescence
HSI Hyperspectral image
IR Infrared
mc-Si multicrystalline Silicon
NIR Near Infra Red
NEO Norsk Elektro Optikk
PPB Parts Per Billion
PV Photovoltaics
PL Photoluminescence
ROI Region Of Interest
SNR Signal to Noise Ration
SRH Shockley Read Hall
STC Standard Test Conditions
SQL Shockley Queisser Limit
SS Solar Simulator
SWIR Short-Wavelength InfraRed
WR White Reference

Contents

Abstract	I
Sammendrag	III
Preface and acknowledgements	V
List of abbreviations	VI
1 Introduction	1
2 Theory	3
2.1 Silicon solar cells	3
2.2 Hyperspectral imaging	9
2.3 Solar spectrum and water absorption	12
2.4 Transmittance and Reflection	13
3 Experimental	15
3.1 Instruments	16
3.2 Exp 1: Laser excitation of cell	19
3.3 Exp 2: Solar simulator excitation of cell	20
3.4 Exp 3: Outdoor conditions long distance	22
3.5 Exp 4: Module imaged in laboratory	25
3.6 Exp 5: Outdoor conditions short distance	28
3.7 Exp 6: Outdoor conditions short distance	29
3.8 Data analysis	30
4 Results and discussion	31
4.1 Infrared module inspection	32
4.2 Excitation by laser and solar simulator on mc-si cell	33
4.3 Luminescence signals from module in lab	38
4.4 Sunlight excitation in outdoor conditions	43
4.5 Discussion of results	56
5 Conclusions	61
Further work	64
Bibliography	68

Appendices	69
A Python script for HSI processing	70
A.1 Example code for data processing	71
B Additional results from data analysis of HSI acquired in Experiment 3: Test Case 3	74

Chapter 1

Introduction

Photovoltaic (PV) solar power has experienced a spectacular growth in the last years. In 2017 the world added 97 GW capacity from solar PV, which was more than from any other type of power generating technology that year [2]. It is also forecasted that by the end of 2023 solar PV capacity will have expanded to almost 600 GW. Today the world total is 402 GW [2] [3]. The installed capacity in the world is increasing and solar PV is becoming a bigger part of the energy mix.

Reviewed literature on PV field performance show an average degradation rate of 0.8%/year, with the median at 0.5%/year (Jordan & Kurtz, 2012). This information, in combination with the forecasted PV capacity, means it is exceedingly important to understand the long-term degradation of installed modules, both to predict when modules need to be replaced and to reduce the effects of degradation at an early stage.

In recent years, several different solar cell technologies have appeared utilizing different semiconductor materials, but silicon still covers the largest technology share. Pure silicon never occurs in nature but use of silicon in semiconductor devices and solar cells demands a purity level in the parts per billion range (PPB). This means that there are several processing steps from the silicon compounds, as silica and oxides, to solar grade silicon. Even though the advances in production and purification technologies have been major the last decades, there is still a lot that is not understood of the effects of how imperfections in production result in degradation and defects in solar cells.

Advanced characterization techniques play an important role in quality testing, process development and optimization in the PV solar industry. Hyperspectral imaging (HIS) of photoluminescence (PL) is a characterization technique that is fast, non-destructive and spatially accurate. There have been several studies on the use of this technique with especially good results when it comes to charge carrier lifetimes, which is the average time it takes for a minority carrier to recombine. Reasons for reduced carrier lifetime

could be many, but material quality is the most important factor.

Luminescence imaging has been a technique that have been researched more and more in recent years for use in PV applications. In 2010 Giescke et al., [4] showed that carrier lifetime down to the timescale of a microsecond can be reliably measured in inhomogeneous materials, e.g multicrystalline upgraded metallurgical grade silicon. In 2011 Datta et al., [5] used PL signals from wafers to quantify surface defects and calculate the solar cell output parameters and link them to the intensity of the PL signal and the defect density on the wafer surface. In 2017 Zhu et al., used inhomogeneous illumination PL imaging to extend the applications of conventional PL imaging to series resistance imaging emitter sheet resistance and diffusion length measurements. These are but a few examples of how this technique has been used for PV applications.

But even though this technique is yielding good results in the laboratory, it poses a challenge when a module is to be analysed; it is not easy to design a module-size light source with sufficient power and appropriate wavelengths for PL imaging.

In 2017 several research groups explored the possibility of imaging luminescence signals from modules outdoor, with various approaches. Silverman et al., [6] explored several techniques of luminescence imaging. They evaluated PV module defects using electroluminescence (EL) indoors, under illumination outdoor EL and open-circuit (OC) outdoor PL. PL images was extracted by subtracting pair of short-circuit (SC) images and OC images taken in close succession to separate the luminescence signal from the background. This technique showed that details like cracks and nonuniformity due to variation of lifetime appear in the PL image. Bhoopathy et al., [7] did a similar PL imaging experiment which also yielded promising results.

The solar group at the Norwegian University of Life Sciences (NMBU) have previously looked at the possibility to characterize the radiative signals to areas of the solar cell. The promising results from this research led to the idea of using this method as an easy and fast application for monitoring degradation of PV modules. To explore this idea further, the instruments and theories had to be tested, so a series of experiments were designed to see if a PL signal could be collected from modules situated outside. The first test cases will be performed in a lab using laser and solar simulator for excitation, these preliminary results will be used as a reference to the results from outdoor experiments. When conducting experiments outdoor many factors of uncertainty are added, such as changes in illumination and strong reflection from the imaged scene. The work has therefore revolved around improving the method of imaging modules outdoor, by enhancing PL signal and reducing noise. By improving the method, we hope to show that HPI of modules situated outdoor in daylight can be used to map degradation mechanisms in PV modules.

Chapter 2

Theory

In this chapter, literature reviews of the relevant fields are presented. Firstly the theory of silicon solar cells is presented. Thereafter, photoluminescence from silicon based solar cells is described before the principles of hyperspectral imaging is explained. Then the possibilities of detecting outdoor photoluminescence signals of photovoltaic modules with sunlight excitation through hyperspectral imaging is discussed. Lastly optical properties of the solar spectrum and PV module are described.

2.1 Silicon solar cells

Most of the world's solar cells are made from silicon (Si). In 1961, William Shockley and Hans-Joachim Queisser at Shockley Semiconductor calculated that the maximum theoretical efficiency for a single p-n junction solar cell with a direct bandgap was 30% at 1.1 eV [8]. An updated value was calculated in 2016 where a more detailed solar spectrum was used which set the limit to 33.16% at 1.34 eV. Si has a bandgap energy of 1.12 eV at 300 K [9], which means that absorbed photons with energies equal or above 1.12 eV can generate an electron-hole pair by exciting an electron from the valence band to the conduction band. Because Si has an indirect bandgap the electron also need to change momentum to reach the conduction band, therefore a phonon is needed in addition to the photon as illustrated in figure 2.1. Materials with direct bandgap is also used as a PV material, like Gallium Arsenide (GaAs). A direct bandgap gives the material a higher generation rate, but it means a shorter carrier lifetime, e.g. the average time it takes for a carrier to recombine, which gives Si an advantage. Si is the second most abundant element in the earth's crust [10] which makes it a cheap raw material and is not toxic so it is easier to handle than GaAs. Solar cells are made up of different types of Si precursors, and different solar cell design have different material requirements.

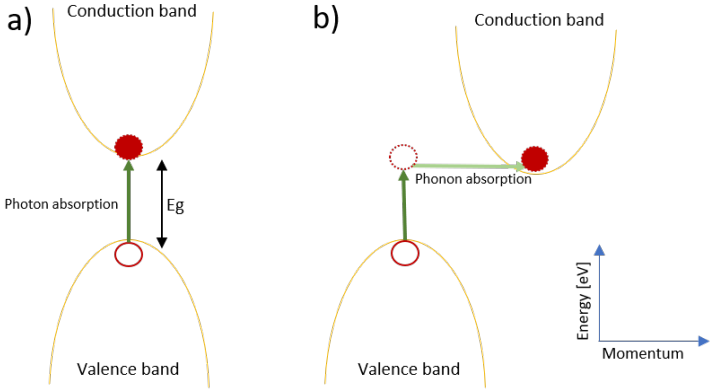


Figure 2.1: An electron in a direct band semiconductor (a) is excited from the valence band to the conduction band by absorbing a photon with energies equal or above the bandgap energy E_g . To excite an electron in an indirect band semiconductor (b), a phonon is needed to change the momentum of the electron, in addition to the absorbed photon, for it to reach the conduction band.

A solar cell is a device that converts the energy in light into electrical energy by the process known as the photovoltaic effect [11]. The basis of this energy conversion is the p-n junction. The junction is formed by the interface between regions of the same material with different dopants, namely holes and electrons. These doped layers are called p-type and n-type respectively, and is the result of a controlled introduction of impurities to the material. The large difference in electron concentration between the n-type and p-type region causes electrons to diffuse from the n-type material to the p-type material and holes diffuse from p-type to n-type material. This diffusion creates ionized dopant atoms and causes the region close to the junction to be almost depleted of mobile charge carriers. This depletion region gives rise to a space charge created by the ionized dopant atoms that creates an electric field gradient that can separate photogenerated electron-hole pairs.

The properties of the junction can also be explained by examining the electrochemical potential in the respective regions. The electrochemical potential describes an average energy of electrons and is represented by the Fermi energy level. By introducing an excess of electrons in a semiconductor material the Fermi energy level will be slightly below the conduction band, and by introducing an excess of holes the Fermi level will be positioned slightly above the valence band, illustrated in figure 2.2a. When the p-n junction is in equilibrium, the Fermi levels will align and the result is band bending of the conduction and valence band, illustrated in figure 2.2b. This band bending creates "wells" for the charge carriers which separates light generated holes and electrons at the junction as it is favourable for them to drift in opposite directions, giving rise to the photovoltaic effect.

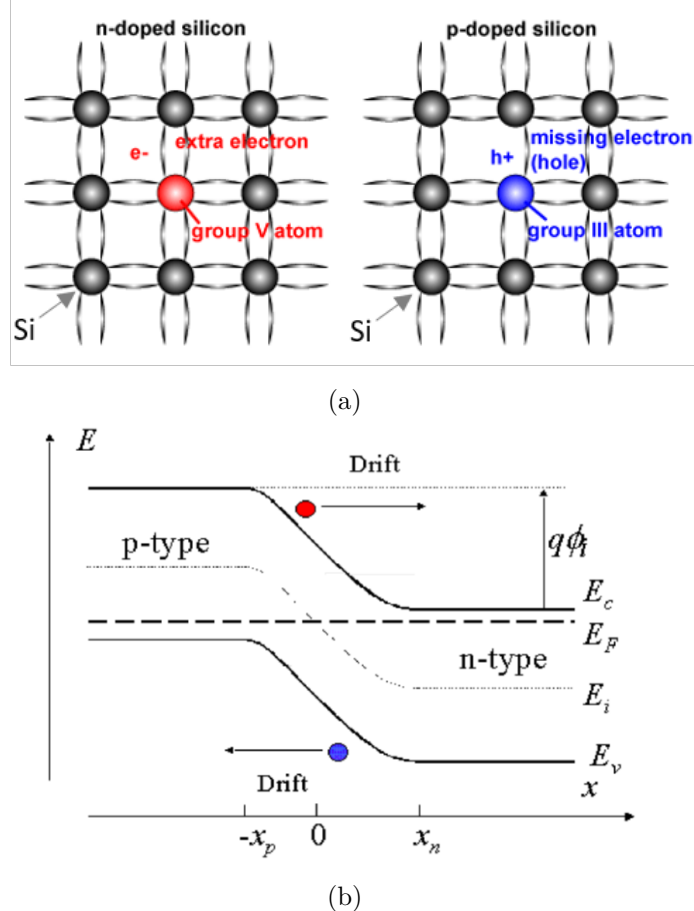


Figure 2.2: Schematic illustration of (a) silicon crystal lattice doped with impurities to produce n-type and p-type material. Illustration adapted from [12]. Energy diagram of a p-n junction in equilibrium (b), with electrons as red dots and holes as blue dots. The depletion region extends from $-x_p$ to x_n , and conduction band, (E_c), valence band, (E_v), and fermi energies (E_F) are indicated. The built-in potential ϕ_i is equal to the work function difference between the n-type and p-type semiconductors. Illustration adapted from [13].

Bias of PN junctions

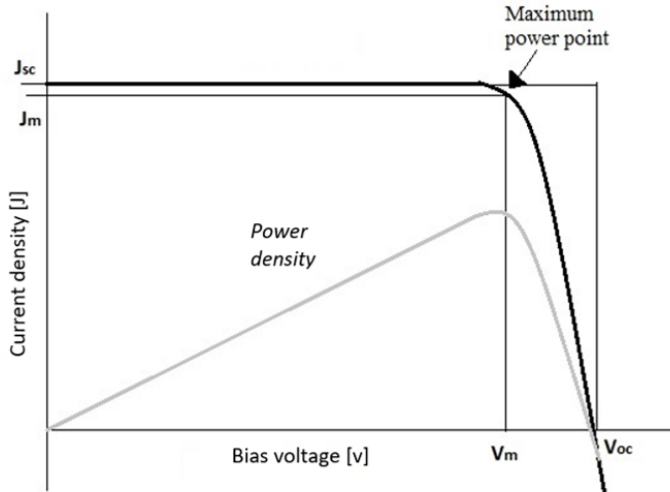


Figure 2.3: The current voltage (black) and power-voltage (grey) characteristics of an ideal cell. The maximum power density is given by $J_m \times V_m$. At short circuit (SC) the current reaches its maximum J_{sc} and the voltage is zero, by increasing the voltage the current continues at its max before V reaches V_m and the current falls sharply until open circuit (OC) is reached where the voltage reaches its maximum, V_{oc} , and there is zero current in the cell.

Semiconductor devices, such as solar cells, has three states of operation. At thermal equilibrium there is no external excitation such as light applied bias, the density of free electrons equals that of holes, and there is no net current in the device. Under Steady State the solar cell has an external excitation that generate charge carriers and the device is no longer in equilibrium. The generated charge carriers will tend to recombine, thus striving to restore the equilibrium state. So, in steady state the rate of charge carriers generated must equal the rate of recombination. Devices typically operate in steady state and are either in forward or reverse bias. If there are rapid changes in illumination or applied bias, there will be a short delay before the solar cell responds, thus the device is in a transient state.

Depending on the bias of the junction a solar cell can either generate or consume power. When a solar cell is subject to an external excitation source, for instance, illumination or forward biasing, the density of free electrons will increase, illustrated in figure 2.3. This causes the electric field at the junction to be reduced. When the electric field is reduced it disturbs the state of equilibrium in the sample, reducing the barrier to the diffusion

of carriers from one side of the junction to the other and increasing the diffusion current. While the diffusion current increases, the drift current remains essentially unchanged since it depends on the number of carriers generated within a diffusion length of the depletion region itself. Because the reduction of the width of the depletion region is minor, there is little to no change in the number of carriers drifting across it. As a result, the device produces power in forward bias operation as long as the potential difference of the junction, E_g , is between 0V and V_{OC} . When the bias voltage is zero, the cell operates at maximum current density (J_{sc}) and almost all carriers are extracted from the cell, leaving only voltage-independent carriers in the cell. At V_{OC} no carriers are extracted from the module and all light generated carriers recombine within the cell, therefore the product of OC-SC values should yield a PL signal.

If the applied voltage is lower than 0 V, $E_g < 0$, the device operates as a photodetector, consuming power to generate a photocurrent which is light dependent but bias independent. If the applied voltage exceeds V_{oc} the device again consumes power. This is the regime where light emitting diodes operate.

Recombination mechanisms

When a piece of semiconductor material is illuminated by electromagnetic radiation with energies over the materials band gap energy, electrons will be excited from the valance band to the conduction band which result in the formation of an electron-hole pair.

The excited electrons will inevitably recombine with holes and annihilate each other. There are several different recombination mechanisms which is important for how the photovoltaic device operates which can be divided into two categories: *unavoidable* recombination processes which are due to the essential physical processes in the intrinsic (undoped) material, and *avoidable* processes which is due to imperfections in the material.

There are 3 recombination mechanisms, illustrated in figure 2.4. Amongst the *unavoidable* recombination processes are the radiative, band-to-band (BB) recombination, where an electron in the conduction band directly combines with a hole in the valence band, and releases a photon similar to the band gap energy and is therefore weakly absorbed and can exit the semiconductor material. The other *unavoidable* process involves 3 carriers and is called the Auger recombination process. When the electron and hole recombine the excess energy increases the kinetic energy of another electron by an amount equal to the band gap. The electron then thermalizes back down to the conduction band edge.

The *avoidable* recombination process is recombination due to material defects called Shockley-Read-Hall (SRH) recombination. The region between the conduction band and the valence band is called the forbidden

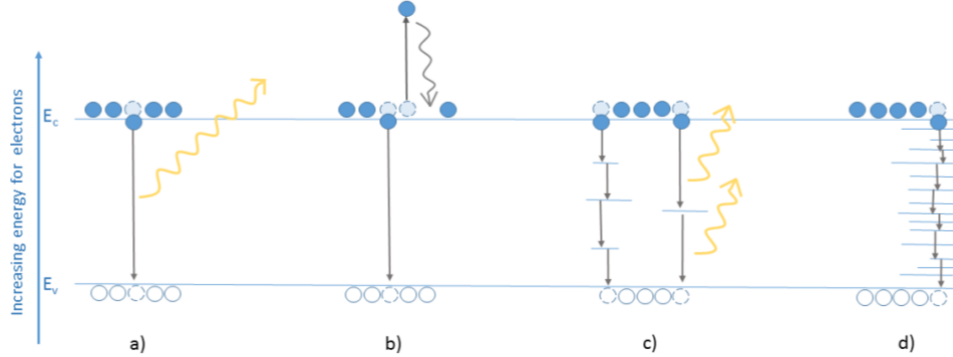


Figure 2.4: Schematic illustration of recombination mechanisms in a silicon solar cell. a) Radiative (BB) recombination, b) Auger recombination, c) SRH-recombination and d) surface recombination. Illustration from [17]

region and carriers cannot have an energy state within this region. Impurities in the crystal or defects in the crystal structure create energy levels, or trap states, in the forbidden region. An electron will first relax from the conduction band to the defect level, and then relax to the valence band where it recombines with a hole. This trap assisted recombination often releases the carrier energy through phonon emission, e.g. thermal energy, but the energy can also be released as a radiative emission where the energy level differs from that of the band gap and is characteristic of defect energy levels [14] [15]. Atoms at the surface of a semiconductor material are more likely to have what is termed "dangling bonds". These are atoms that do not have enough electrons to fill up their valence shell, and would be called "free radicals" had they not been immobilized in the crystal lattice. These dangling bonds induce SRH recombination by creating trap-states, as illustrated in figure 2.4 d), and affects the solar cell performance greatly. A way to reduce the number of dangling bonds is by adding a passivating layer at which silicon nitride is commonly used [16].

2.1.1 Luminescence imaging

Luminescence is a materials ability to spontaneously emit electromagnetic radiation after absorbing energy in various forms. This energy emission can be recorded in an image if the wavelength is within the range of the camera sensors.

Photoluminescence

The spontaneous emission of light as a result of absorbing photons in the radiative recombination is called photoluminescence.

Electroluminescence

When external carriers are injected through contacts in the cell, they eventually recombine and emit what we refer to as electroluminescence (EL). To produce EL the cell needs to be connected to an external electric power source. In recent years what has been known as contactless EL has emerged as an alternative technique to the traditional EL for examining cells. As the name implies, this is done without connecting the cell to a power source, but instead a cell is only partly illuminated, and the non-illuminated part is imaged. This way carriers are generated in the illuminated areas and act as carrier injections in the non-illuminated regions. Studies have shown that contactless EL provide very similar images as conventional EL, but has the potential to be employed as automated and/or remote acquisition for outdoor arrays [18].

2.1.2 Photoluminescence and defect luminescence in silicon

To make solar cells out of silicon the silicon needs to be of a purity level in the parts per billion (PPB) range. Impurities in the material causes defects in the solar cell and lowers the solar cells efficiency. Crystal defects such as vacancies, dislocations and substitutional atoms will also contribute to the loss of efficiency. These defects can create energy trap states in the solar cell material and result in SRH recombination. These radiative signals is called defect related luminescence (DRL) and was first described by Drozdov et al. in 1976. The DRL signals Drozdov et al. found is associated with dislocation defects and is referred to as D-line signal. The names and respective energy levels are D1 at 0.812 eV, D2 at 0.875 eV, D3 at 0.934 eV and D4 at 1.000 eV. Other DRL signals have later been reported at D5 at 0.826 eV [19], D07 at 0.694 eV [20] and VID3 at 0.94 eV [21].

As DRL is an indication of a material defect, BB radiation indicates high material quality. Even though it is unlikely to record DRL signal outdoor, the intensity of BB radiation can provide material quality information. In areas void of BB radiation, it is likely that the solar cell has a material defect, e.g. *bad* cell area, and where there is high intensity BB radiation the material has few defects, e.g. *good* cell area.

2.2 Hyperspectral imaging

Hyperspectral imaging is a technique that combines images with spectroscopy. A hyperspectral image divides the electromagnetic spectrum into bands where every band has a range of wavelengths. Usually a hyperspectral camera has dozens or hundreds of bands so that a contiguous electromagnetic spectrum from each spatial position is obtained [22]. The operating principal of a hyperspectral camera: the entrance aperture and lens, images the

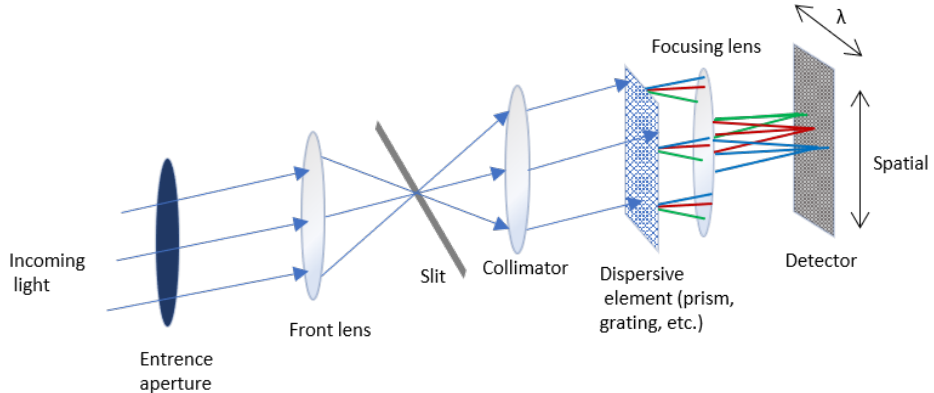


Figure 2.5: Operating principle of a hyperspectral camera: the entrance aperture and lens, images the scene onto a slit which only passes light from a narrow line in the scene. The incoming photons are aligned by the collimator before a dispersive element separates the different wavelengths and the light is then focused onto a detector array.

scene onto a slit which only passes light from a narrow line in the scene. The incoming photons are aligned by the collimator before a dispersive element separates the different wavelengths and the light is then focused onto a detector array, as shown in figure 2.5.

A hyperspectral image consists of images of the same object, one for each band, stacked on top of each other. These three dimensional multivariate data structures are called hypercubes, illustrated in figure 2.6, and has two spatial dimensions (X, Y) and one wavelength (λ) dimension [23].

Pushbroom Scanner

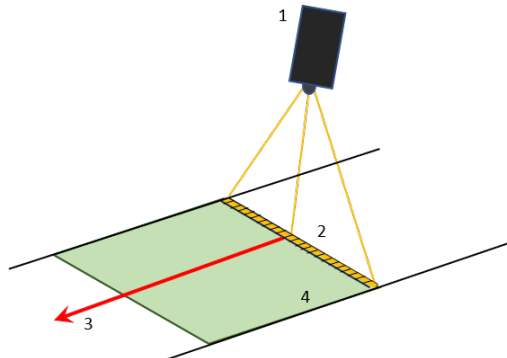


Figure 2.7: A pushbroom scanner uses a line detector to image one pixel line (2) at a time in the direction of the red arrow (3) by moving either the sample holder (4) or the camera (1).

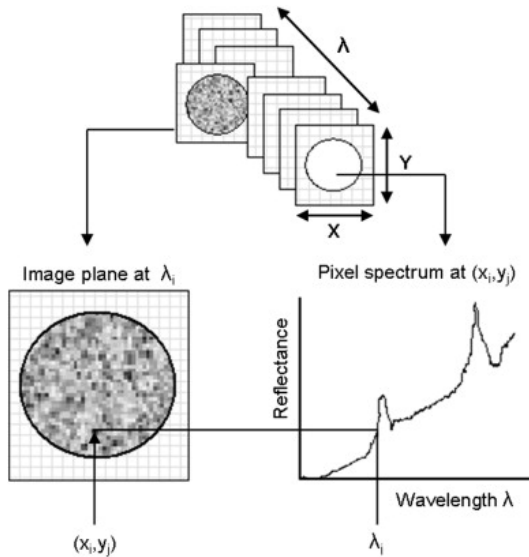


Figure 2.6: A hyperspectral image cube, 'hypercube', consists of stacked 2D images, one for each spectral band, where each pixel in the 2D image represent the photon count for that wavelength in that spatial position. Illustration adapted from [23]

The camera images the sample by using a line of detectors arranged perpendicular to the sample. By moving either the camera or the sample one spatial line is imaged at a time as illustrated in figure 2.7. The line is split into its spectral components before reaching a 2D sensor array where one dimension is used for spectral separation and the other is used for imaging in one spatial direction. The result is a 2D image for each spectral band.

Count and resolution

The detector array of the hyperspectral camera is a charged coupled device (CCD). The CCD converts incoming photons from a scene to a digital signal. A photon hitting a pixel knocks loose an electron, and hence deposits a charge on the pixel. The charge on each pixel is thus a measure of the number of photons which struck it. The efficiency of this capture, or the probability that a photon generates an electron, is called the Quantum Efficiency (QE) of the device. These photoelectrons are then converted into a numerical value, usually referred to as "data number" or simply "count". The conversion factor between the produced electrons and the count is called the "gain" of the CCD.

In theory, if the shutter is closed and an image is captured with a short exposure time, there should be no photons arriving at the CCD. However, in reality the count will not be zero. This is due to the presence of thermal

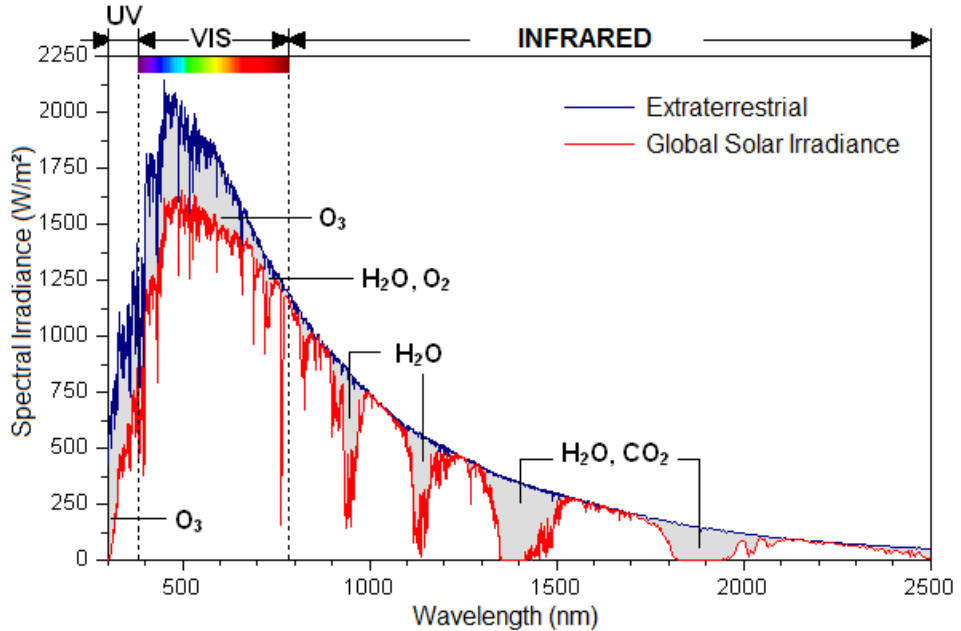


Figure 2.8: Standard solar spectrum adapted from [25] showing global and extraterrestrial solar irradiance. The difference between these spectra are gases in the atmosphere that absorb radiation at different wavelengths, as indicated in the figure.

noise, "dark current" and the CCD bias. The bias represents the individual pixel-to-pixel variations of the offset level. The bias often has some sort of pattern across the CCD, and does not appear random. Due to the thermal energy of the material lattice of the CCD, electrons are generated over time that are independent of the light falling on the detector, and due to their movement some charge is deposited in the pixels. This dark current is reduced by cooling the CCD, and around 163 K the dark current is usually negligible [24].

2.3 Solar spectrum and water absorption

Solar radiation is electromagnetic radiation from the sun. The average extraterrestrial irradiance flux from the sun that hits the earth's outer atmosphere is known as the *solar constant* and has a value around 1365 W m^{-2} [26] with yearly and cyclic fluctuations. Figure 2.8 shows the electromagnetic spectrum. The difference between the extraterrestrial and global solar irradiation is electromagnetic waves that have been absorbed in the earth's atmosphere before reaching the surface. There are some areas of the global spectrum, illustrated in figure 2.8, that have significantly lower spectral irradiance due to absorption. These absorption gases are mainly ozone (O_3),

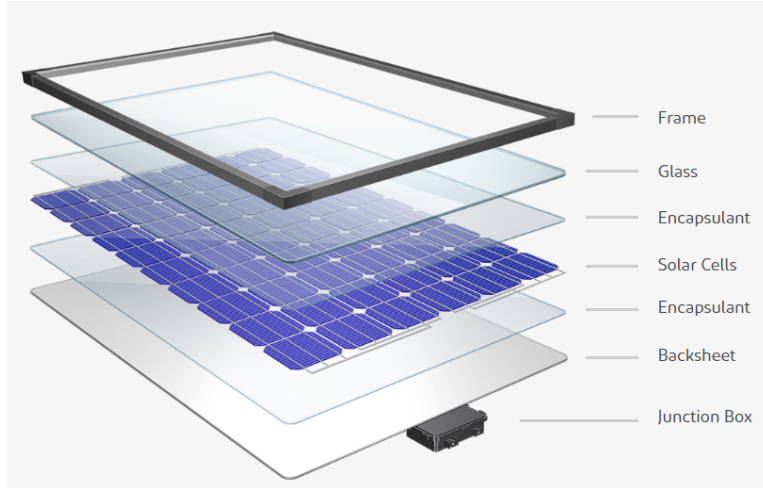


Figure 2.9: A photo voltaic module consists of several material layers, where the most important layer in terms of reflection is the cover glass. Image credited to Novergy Solar [29]

carbon dioxide (CO_2) and water vapor (H_2O). Water vapor is by far the most abundant gas of these three, especially close to the earth's surface, and varies with time and space, which means absorption rates could vary depending on location and the time of day and year. The BB signal of silicon is approximately 1100 nm, this coincides with an area of water absorption, which obscures signal recordings. Because the signal is so small it could be absorbed by water vapor if the humidity is great or the distance between the signal and the camera sensor is big.

2.4 Transmittance and Reflection

The optical properties of solar cells are key characteristics for the performance of the cell. To increase the photogeneration a solar cell must trap as much light as possible and avoid excessive transmission. Bare silicon has a surface reflection of over 30% [27]. To reduce this, common practice is to apply an anti-reflective coating and texturing. Texturing means roughening the surface to increase the chances of reflected light to bounce back onto the surface, rather than out to the surrounding air. An anti-reflective coating is usually deposited as a thin film ($\approx 75 \text{ nm}$), typically silicon nitride by PECVD (Plasma-Enhanced Chemical Vapor Deposition). A high quality reflective layer can improve the efficiency of the solar cell even by 30% [28].

To utilize solar cells for power production, they are put into a module. The primary function of a module is to protect against mechanical damage, supply electrical insulation and supply chemical and UV protection, it also increases the output voltage, ease installation and ensures reliable solar cell

operation. The most common PV-module have 60 to 72 interconnected solar cells and produces approximately 300 W. A module consists of several layers as illustrated in figure 2.9, but as reflection goes the most important layer is the cover glass. The cover glass offers high transmittance and low reflectivity in addition to strength and durability. The transmittance is typically 92% [30].

Chapter 3

Experimental

To explore the method of using hyperspectral imaging to detect PL signals, a series of experiments were conducted. The first 2 experiments were done in a laboratory under controlled conditions. The results from these experiments was used to design outdoor experiments. With each experiment a little more knowledge was gained, and so a new experiment was designed, in hopes of improving the results further. In this section the experiments are presented in the order they were performed, where experiment 1 was the first to be conducted, and experiment 6 the last. To better understand the methods, the specific instruments used with the experiments are described first. In table 3.1, the experiments are listed along with which camera, sample and carrier injection that was used in the experiment.

Experiment	Camera	Sample	Carrier injection
1	Specim SWIR	Cell 1 and 2	Laser
2	HySpex SWIR-384	Cell 1	Solar Simulator
3: Test case 1	HySpex SWIR-320i	Module A and B	Sun
3: Test case 2	HySpex SWIR-320i	Module A and B	Sun
3: Test case 3	HySpex SWIR-320i	Module A	Sun
4: Test case 1	HySpex SWIR-320i	Module A	Solar Simulator
4: Test case 2	HySpex SWIR-320i	Module A	Current source
5	HySpex SWIR-320i	Module A	Sun
6: First	Specim SWIR	Module A	Sun
6: Second	Specim SWIR	Module A	Sun

Table 3.1: Overview of the experimental work

3.1 Instruments

3.1.1 Light sources

Laser

For experiment 1, a 808 nm line laser, Lasiris Magnum II (Coherent, USA) was used for excitation. This is a high-power laser diode line generator with adjustable beam power up to 5600 mW and a fixed fan angle of 30 degrees. It generates a uniform, non-Gaussian, intensity distributed line. In a 500 μm resolution setup, this gives an irradiation power density of up to 2 W/cm².

Solar Simulator

The SUN 2000 Solar Simulator model by ABET Technologies was utilized with a 550 W Mercury based arc lamp in experiment 2 and 4: test case 1. The solar simulator was equipped with a AM1.5G filter. AM1.5G stands for Air Mass 1.5 global radiation and is the spectra used under standard test conditions (STC) to indicate the performance of PV modules. The number after AM refers to the direct optical path length through the earths atmosphere expressed as a ratio relative to the zenith path length.

3.1.2 Irradiation measurements

To measure the global radiation, which is the sum of direct and diffuse radiation from the sun in the wavelength area 295-2800 nm falling on a horizontal surface, two pyranometers were used.

Rig pyranometer

In experiment 3 a pyranometer produced by *Kipp and Zonen* model CMP6 was used as part of the Rig setup. The instrument is calibrated and measured to have a sensitivity of 16.94 $\mu\text{V/Wm}^2$.

Pyranometer at Sørås weather station

For experiments 5 and 6 a pyranometer located at Sørås was used. The instrument is manufactured by Eppley Precision Pyranometer with a instrument uncertainty of $\pm 10\%$. The Pyranometer is part of a weather station located 800 m southeast from the TF-building where the measurements for this thesis was done.

3.1.3 Cameras

Three different hyperspectral cameras were used during the experiments to allow for different setups. For the experiments on modules the same IR-camera was used in all experiments.

Specim SWIR

For image capture in experiment 1 a near-infrared (NIR) pushbroom hyperspectral camera, SWIR, from Specim, with a mercury cadmium telluride (HgCdTe) detector, has been used. The camera has a spectral distribution from 929.11 to 2530.70 nm divided between 256 spectral bands. Interval widths vary from 6.32 nm for the shortest wavelengths, to 6.23 nm for the longest wavelengths.

Since the Specim SWIR camera detection range is from 930 to 2500 nm, a longpass filter is placed in front of the camera lens when doing recordings with the 808 nm laser to block out reflection from the laser. A longpass filter blocks for shorter wavelengths and allows longer wavelengths to transmit (pass) through.

HySpex SWIR-384

The HySpex SWIR-384 is a hyperspectral camera delivered by Norsk Elektro Optikk (NEO). It is equipped with a mercury cadmium telluride (HgCdTe) detector with a spectral range of 1000 nm-2500 nm and a spatial range of 384 pixels. The spectral range is divided into 288 bands with a spectral sampling of 5.45 nm.

HySpex SWIR-320i

The camera is a HySpex SWIR-320i from Norsk Elektro Optikk with 145 spectral bands that cover the wavelength range 900 - 1700 nm with an indium gallium arsenide (InGaAs) detector. The spatial resolution of the camera is 320 pixels in width.

Optris IR

To acquire infrared (IR) images, the thermal imager Optris PI 640 was used. It's optical resolution is 640x480 pixel with a spectral range of 7.5 - 13 μm and a temperature range of 253 - 1073 K. The images were acquired by taking snapshots of the sample in a set time-interval.

3.1.4 Samples

Cells

Cell 1 and 2 is produced by DelSolar model D6R multi-crystalline Photovoltaic Cell dimensions 156x156 mm and thickness of 200 $\mu\text{m} \pm 30 \mu\text{m}$ with silver busbars, a silicon nitride antireflection coating and a aluminium back surface field. Under STC the efficiency rating is up to 18.6 %.

Rig module

The module is from ITS model: ITS 220ECR4 and consists of 1 string with 60 cells in series. There are 3 substrings with 20 cells in series each. The glass of the module has an antireflective coating provided by Sunarc Technology.

Module A and B

Module A and B is produced by SweModule model Inceptio 250 field and consists of 1 string with 60 cells in series. There are 3 substrings with 20 cells in series each. It has a nominal power output of 250W, short circuit current of 8.80 A and open circuit voltage at 30.3 V measured at STC. To the extent of my knowledge, the modules have not been exposed to sunlight since production and have been stored in a shed at NMBU for the last couple of years.

3.1.5 White reference

PV cells luminescence at wavelengths near their band gap energy. Because the sun emits strongly in the same wavelengths a way to separate the relatively weak signal from the background signal, which may be hundred or thousands of times stronger, is needed. To do that, a white reference is utilized. Adding a white reference to the scene will give a measure of the diffuse reflectance that can be used to separate the luminescence signal from the reflecting radiation.

Spectralon is a fluoropolymer and has a diffuse reflectance of over 90% and > 99% in the range 400 to 1500 nm [31], which is the highest rating of any known material. For experiment 2 a Spectralon stick was placed next to the cell, and in experiment 3: Test case 3 a Spectralon plate was used. By adding carbon various grey levels are achieved, which was the case for the plate used in experiment 5. The reason for not using pure Spectralon in this situation was to achieve longer integration time without saturating the white reference.

3.2 Exp 1: Laser excitation of cell

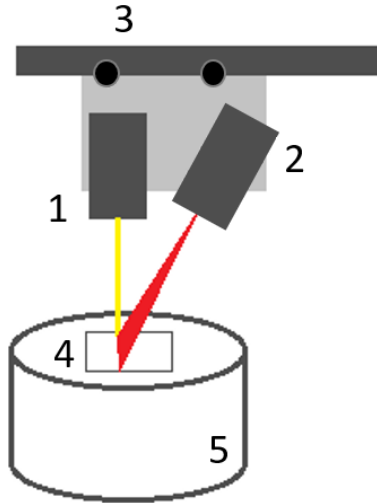


Figure 3.1: Setup for experiment with 808nm line laser (2) and Specim SWIR camera (1) positioned on a linear translation stage (3). The sample holder (5) can cool samples (4) down to 90K by filling it with liquid nitrogen.

In this experiment a line laser, Lasiris Magnum II, was used as excitation source. The line laser emits an energy beam of 808nm in wavelength, which converts to 1.53eV by the equation 3.1.

$$E = \frac{hc}{\lambda} \quad (3.1)$$

where E is energy in eV, $h = 4.135667516 \times 10^{-15}$ eV*s is Planck's constant, $c = 299792458$ m/s is the speed of light and λ is wavelength in meters. 1.53 eV is well above the band-gap energy of silicon which varies between 1.17 eV at 0 K to 1.12 eV at 300 K [9]. The Specim SWIR camera is fastened to a horizontal translation stage with the line laser and positioned directly above the sample holder, figure 3.1. The whole setup is placed inside a black chamber designed to be light-tight during scans. This method has been tested and verified as a viable method to characterize solar cell materials [32]. For cooling the samples to 90 K, a cryogenic container filled with liquid nitrogen was used. The outside of the container is covered with a thick layer of extruded polystyrene foam for isolation, except for the top part where a plate of polished aluminium is situated. The plate is 156 x 156 mm² in size which is adequate for wafers and solar cells so that the entire sample comes in contact with the plate. From the top of the container, heat

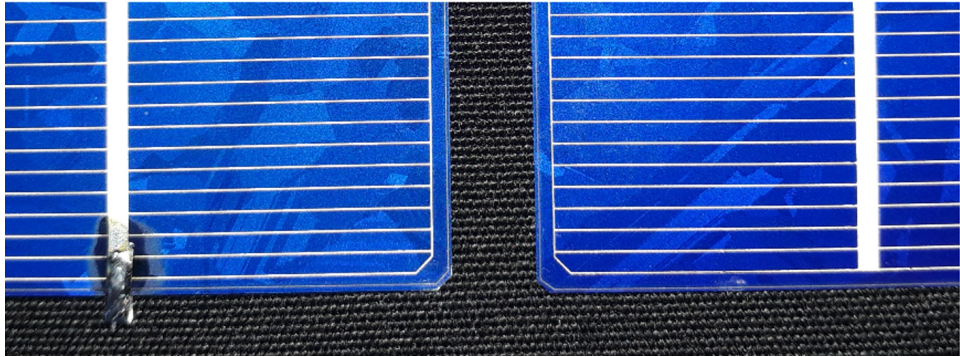


Figure 3.2: Cell from Open Circuit (right) to Short Circuit (left) by soldering the front and the back together.

sinks run down into liquid nitrogen inside the container. Small nozzles are placed on the top of the container and to transport and pour cold nitrogen vapor over the sample. This way the sample cools down in seconds and thermal equilibrium is achieved.

The tank holds up to two litres and the temperature will remain constant until all the liquid nitrogen has evaporated. To control the temperature a thermometer is attached to the surface of the cryogenic container, measuring the temperature of the sample.

The cryogenic container is also used as a sample holder for image capture at room temperature, but then it is not filled with liquid nitrogen. The container was manufactured locally at NMBU. The solar cell was carefully placed in the sample holder and positioned to be in line with the linescanner of the camera before the focus was adjusted. The sample was scanned 3 times in OC before it was cooled down to 90K, reaching thermal equilibrium and scanned 3 more times. In thermal equilibrium the number of phonons available in the material will decrease, and the free charge carriers will tend to occupy the lowest energy states available, e.g. defect related energy states. The sample was then short circuited by soldering the front and the back together, as seen in figure 3.2, before the process was repeated.

3.3 Exp 2: Solar simulator excitation of cell

The procedure in this experiment is close to what was done in experiment 1, but the excitation source is now a solar simulator. The solar simulator emits photons in a range of energies where some will be below the band gap of silicon. The sample is scanned in room temperature, and due to the presence of phonons it is not expected to see DRL signal in this setup.

Cell 1 was placed on the sample holder as illustrated in figure 3.3. A lens with a fixed focus is attached to the camera, so the height of the sample

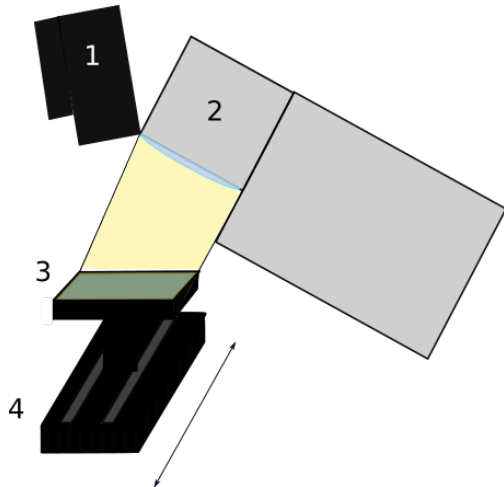


Figure 3.3: Experimental setup with solar cell illuminated by solar simulator (2). Sample holder (3), a square disk covered with black textile, fixed to a motorized, linear translation stage(4). The camera used in this setup is a HySpec SWIR-384 and is positioned vertically above the disc (1).

holder must be adjusted to get the sample in focus. The WR was placed next to the sample. The solar simulator was positioned so that it illuminated a cell and the WR, but as figure 3.3 illustrate, the solar simulator is positioned at an angle. This results in a non-uniform illumination across the sample and the area closest to the solar simulator has a higher irradiation.

Because the width of the linescanner do not cover the whole cell, the cell is re-positioned and scanned again. These positions will be referred to as pos 1 and pos 2. Before scanning the cell, it was carefully aligned with the line scanner, and the height of the sample holder was adjusted to get the sample in focus. For every position three images were taken, first in OC and then in SC.

3.4 Exp 3: Outdoor conditions long distance

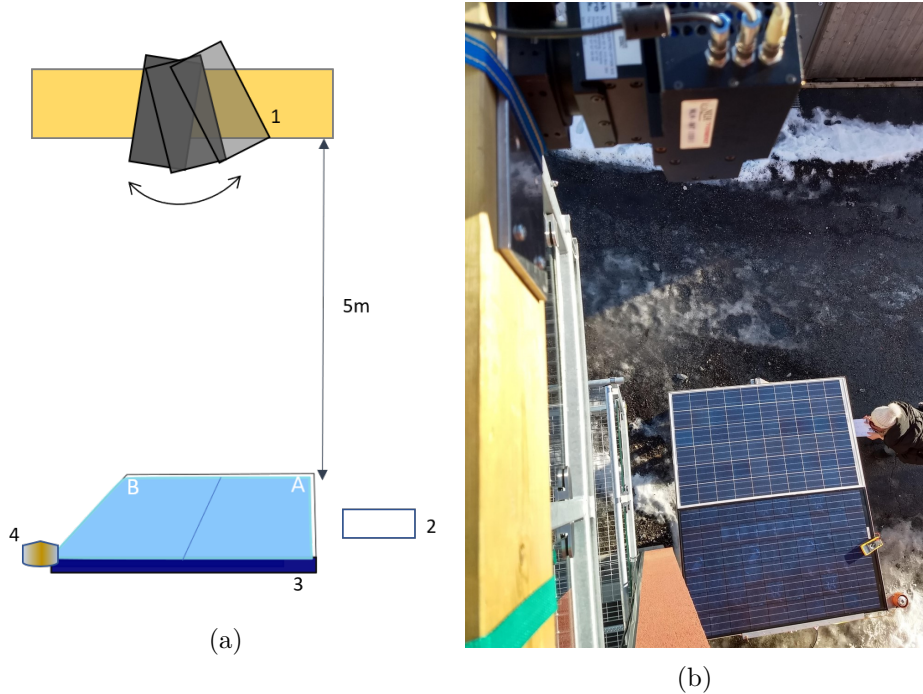


Figure 3.4: Imaging setup for experiment 3: outdoor long distance a). Hypspx SWIR-320i (1) points down on the modules (3) and the white reference (2) is positioned next to the modules. The Pyranometer (4) measures irradiation. b) shows an image taken while acquiring data in experiment 1.

Experiment 3 is divided into 3 test cases, where the technique changes based on experiences during measurements. For these images the HySpex SWIR-320i was used. The sample holder was a wooden frame with a pyranometer from Kipp and & Zonen and the camera was fastened onto a wooden plank with a motorized rotational translation stage. The camera-setup was then mounted onto a railing so the camera was positioned directly above the PV-modules as shown in figure 3.4. The WR was only used in test case 3.

3.4.1 Test case 1: Imaging of same cell in OC and SC with change in illumination

Images were taken of the rig panel in a range of voltages between SC and OC conditions. First a calibration picture for the background was taken. The rig module was connected to a resistance box, where voltage and current can be adjusted. By adjusting the voltage, the maximum potential difference in the cells, e.g V_{OC} , was reached, giving a voltage output of 35 V. The module

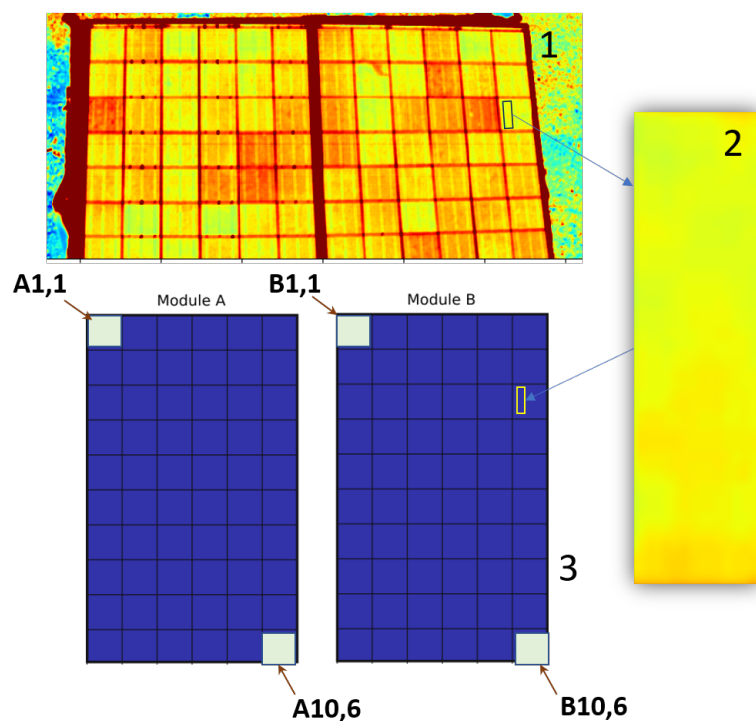


Figure 3.5: When analysing the images an area of a cell, without busbars (2) is extracted from the hyper spectral image of the modules (1). The cells are indexed as illustrated in (3), where the cell area (2) corresponds to the cell indexed as B4.6 in (3).

was scanned, before the voltage was adjusted down by intervals of 2 V, and the module was scanned again. This process was continued until an output voltage of 0 V was reached, the equivalent of a short circuit. For every image taken, the irradiation, current and voltage was noted. Because of changes in irradiation during the measurements, which will affect the signal intensity and reflection, the voltage was turned up again to attain an OC image closer in time and radiation to the SC image. Lastly IR images were obtained by using the Optris imager.

3.4.2 Test case 2: Imaging of different cells in OC and SC with same illumination

Test case 2 yielded no PL signal but strong radiative reflection, this test was therefore adapted accordingly. In this method two modules, module A and module B, was scanned with module A in OC and module B in SC. A series of 5 images was acquired and the illumination was measured by the Rig pyranometer for every scan.

3.4.3 Test case 3: Imaging of same cell in OC and SC with Spectralon plate

The results from test case 2 revealed that the signal to noise ratio was low. To eliminate as much noise as possible a Spectralon plate was placed beside the modules ((2) in figure 3.4) so that the images could be corrected for diffuse and specular reflection. Both panels were scanned in OC and SC, in order to analyse the same cell in both situations, to reduce uncertainties. To further increase the signal to noise ratio 20 images was taken in each situation (OC/SC), to reduce the effect of changes in irradiation.

3.5 Exp 4: Module imaged in laboratory

After processing the images acquired outside, it was clear that the method had to be modified even further to capture the BB signal. To do that more images needed to be taken in a controlled environment. The solution was to take the whole module into the lab.

To increase the sensitivity of the camera, a lens was attached to the camera so that the ideal distance between the lens and the sample was 1 meter. The camera was then fastened to a frame in the lab so that there would be 1 meter between the module and the camera. The solar source was placed on the opposite side of the panels from the camera.

For the EL images the panel was connected in parallel to a current sources as illustrated in figure 3.8 otherwise the setup remained the same.

Test case 1: Solar Simulator

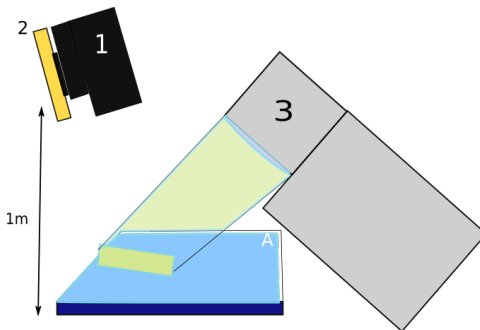


Figure 3.6: Experimental setup of experiment 4 (a), (1) Hypspex SWIR-320i camera, (2) rotational translation stage and (3) the solar simulator.

To acquire PL images the module was illuminated by the SS. The SS had an effect input of 450 W and the irradiance was measured with a RERA solutions silicon reference cell. Because the SS was positioned at an angle towards, illustrated in figure 3.6 the module the irradiation was not distributed evenly over the illuminated cells, therefore two measurements were done in the near and far end of the illuminated area. These measurements was 35.6 mV and 38.9 mV respectively. The reference cell is calibrated to have a voltage over the shunt of 93.7 mV When illuminated by 1 sun (1000 W/m^2 air mass 1.5G). By assuming the reference cells quantum efficiency (QE) is linear in regards to irradiation intensity, the irradiance from the SS can be calculated to be 381 W/m^2 and 415.15 W/m^2 . This approach is not the ideal way to measure irradiance, to assume that the electric components responds linearly to changes in irradiation is incorrect, but this approach gives an inclination of which irradiation levels the module experiences. Ideally the SS would produce a spectrum similar to the solar, but as the HSI

was analysed we found the spectra reflected by the WR to be closer to what is shown in figure 3.7.

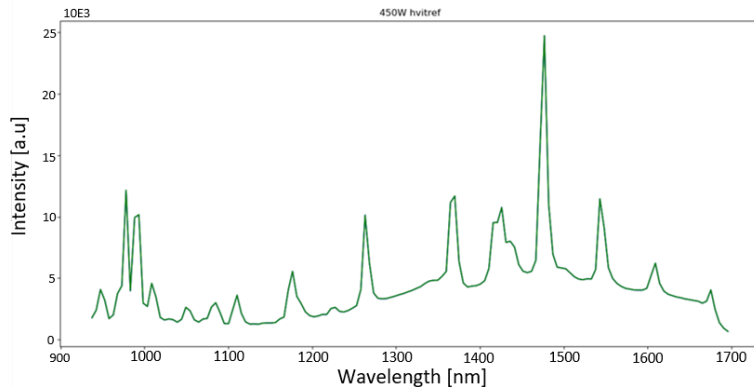


Figure 3.7: Spectra of the reflected irradiation from the white reference.

3 images were taken of 3 different cells in OC and SC, amounting to a total of 12 images. The imaged cells were chosen among cells in column 1, situated directly beneath the camera, that did not heat up in the IR-images from experiment 3 due to power dissipation.

Test case 2: Electroluminescence

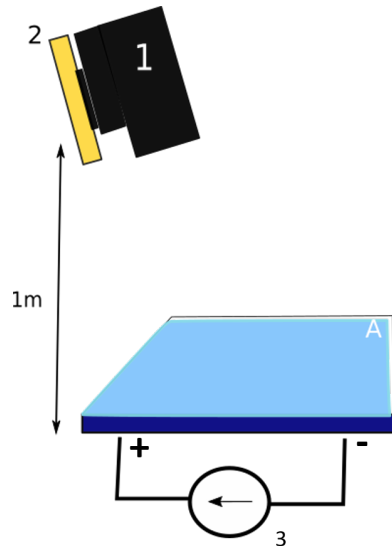


Figure 3.8: To measure EL, the camera (1) was fastened to a rotational translation stage (2) 1 m above the module, and a current source (3) was connected in parallel to the module to apply a forward bias on the cells.

Module imaging based on EL is a commonly used technique to detect defects in solar cells. EL images are collected by driving a current through the module in forward bias in a dark environment.

First, a test of the setup was performed by connecting Module A to a current source. Cell A5,2, A4,2 and A8,2 was scanned. In this test there was sunlight coming from the windows, so to override the generated current in the Module it was covered by black textile while the current source was applied. When the current and voltage stabilized the textile was removed. Each of the 3 cells was scanned 5 times with a white reference.

After analysing the images some modifications were made. A current source was connected in series with the existing two to increase the applied current. To avoid light pollution from the windows the experiment was performed in the dark.

Cell A8,2 was scanned in complete darkness, first with a current of 8.95 A and voltage of 4.02 V. The electrical instruments started to generate heat due to the high current, and to avoid overheating one of the current sources was removed for the next series of images. 10 more images were taken of cell 3 with a current of 1.66 A and a voltage of 35.2 V. During this experiment there was some technical issues with the software operating the camera, consequently only cell A8,2 was imaged. Scan 4 of the series was corrupted due to crash of the software.

3.6 Exp 5: Outdoor conditions short distance

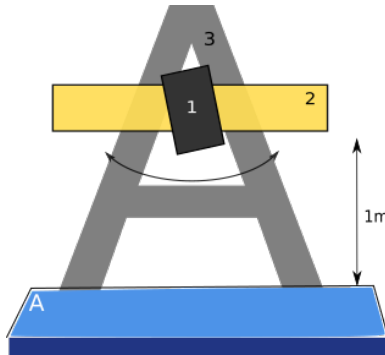


Figure 3.9: Experimental setup of experiment 4. Camera (1) is fastened to a rotational translation stage (2) which is mounted on a step-ladder (3) 1m above the module.

Due to promising results in experiment 4, this experiment is designed as a replica of that, but situated outdoors. The location was a rooftop of one of the university buildings to avoid shade and to have a big area to work on. The camera was fastened 1 meter above the ground to a stepladder which was secured to a railing. Module A was placed on a level ground below the camera as shown in 3.9. In this setup only one cell could be imaged at a time, together with the grey Spectralon plate. The Opiris IR imager was used in between scans to make sure that no shade from either the Spectralon plate or surrounding cords and instruments fell on the module, which could cause mismatched currents between the cells in short circuit.

Except for a change in the setup of equipment, these images were taken in the same manner as experiment 3, first the module was in OC then in SC. During recordings the module was inspected with the IR camera. Because the cameras field of view was limited, the WR had to lie on the panel while the image was recorded. This proved a challenge in SC conditions because the moment the WR covers a cell, the cell goes into backwards bias and a great deal of power is dissipated in the covered cell. This reduces the current in the string greatly, and we could get a situation close to OC. To avoid this, the WR was placed on a cell in the neighbouring string. This was done for cell A8,2 and cell A6,1, for cell A5,1 this was not possible, instead, the WR was placed directly on top of cell A5,1 after an image was taken, and then an image was taken of the WR. The irradiation conditions this day was quite stable, so even though the image of the WR was not taken shortly after the cell image, an assessment was made that the conditions would be similar enough to use the WR images to correct for reflection.

During data collection the pyranometer at Sørås measured irradiation between 524 and 538 W/m². The sky was cloudless so these measurements



Figure 3.10: Image taken of instrument setup for experiment 6. Specim SWIR camera is fastened to a linear translation stage directly above the module.

should be applicable to the conditions on the roof.

3.7 Exp 6: Outdoor conditions short distance

Because of a suspicion that there might be a systematic error in the HySpex SWIR-320i camera, an experiment with the Specim SWIR camera was performed. The camera was, as before, mounted to a linear translation stage and placed directly above module A on the roof of an university building (same location as experiment 5) at a distance of 1m, image of this setup is shown in figure 3.10. The grey Spectralon plate was placed on the ground next to the module to be in the cameras view along with row 1 of module A. Images was acquired over two days, eight days apart. The integration time, the time it takes for the detector of the camera to collect the photons, varied between 10 ms to 18 ms.

During the first data collection the Sørås pyranometer measured irradiation between 604 and 618 W/m². During the second data collection the measured irradiation was between 314 and 461 W/m².

3.8 Data analysis

To analyse the hyperspectral images several processing steps was done using Python as programming language. The processing technique can be divided into 5 steps as illustrated in figure 3.11. For data acquisitions without WR step 3 is skipped. ROI is primarily a cell area without busbars, a white area under module glass or an area of the WR. An example code is presented in appendix B.

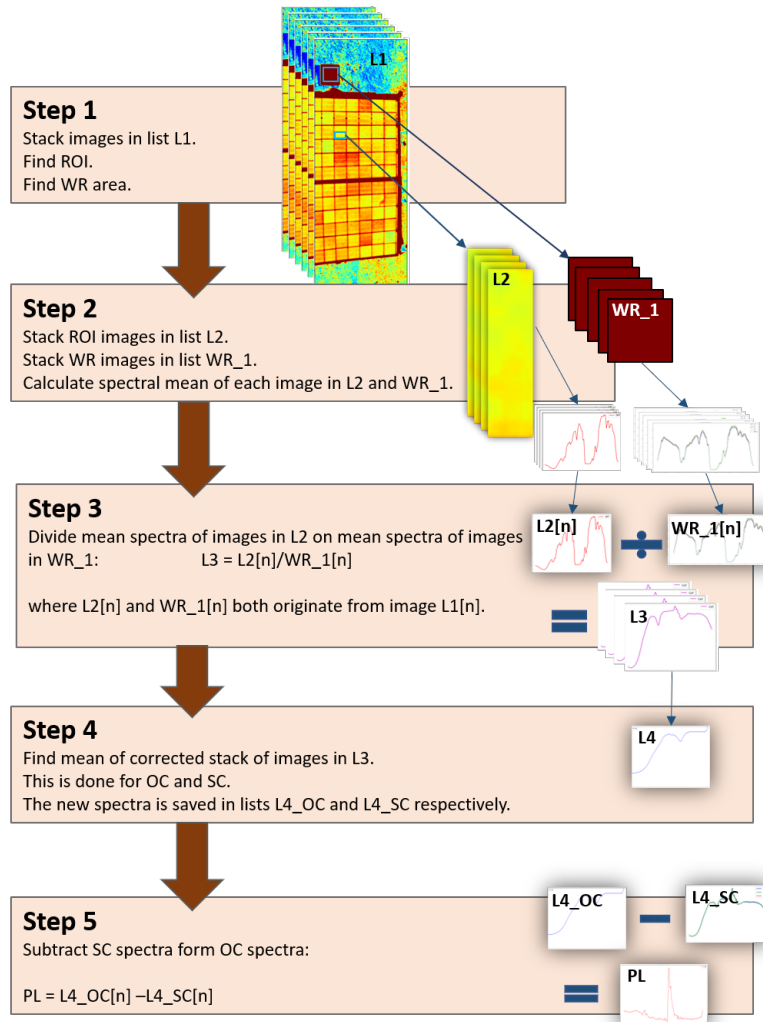


Figure 3.11: The basic script for analyzing images involves 5 processing steps. The text boxes describes the algorithm and the illustrations to the right is made to resemble the output from each step.

Chapter 4

Results and discussion

The main goal of this thesis was to explore the method of using hyperspectral imagining of PL signals to detect degradation of PV modules. The starting point was to review examples of methods that have been used to detect PL signals before, elaborated in the introduction chapter. Next experiments where mc-Si solar cells was illuminated with a 800 nm intensity line laser and with a solar simulator of a cell in OC and SC conditions was conducted. The next goal was to detect this signal outdoor, from a commercial module with mc-si solar cells in daylight. The experiments were based on previous research done by Burud et al, 2013. This chapter discusses strength and weaknesses of the methods and how variations in the experimental setup affected the results, before the results are evaluated and the outlook for using this method for PV applications is described and discussed. This thesis is related to previous work in the solar group, especially by T. Mehl [32], I. Burud et al. [21] and Bhoopathy et al. [7]. T. Mehl demonstrated in his Ph.D which radiative signals can be detected in the setup of experiment 1 while Burud et al. looked at the possibility to characterize the radiative signals to areas of the solar cell. This promising result led to the idea of using this method as an easy and fast application for monitoring degradation of solar cells. It was evident that moving from the lab to the outdoors introduced many unknown factors and this thesis addresses the development and challenges following this transition.

This chapter presents a selection of results from each experiment, before said results are commented and discussed. The focus of the chapter is to evaluate what can be characterized as noise and what can be characterized as a radiative signal from the solar cell material. The analysing process had the purpose of extracting the PL signal from noise caused by specular and diffuse reflection, and variations in irradiation.

During the analysing work on the images from HySpex SWIR-320i, it was evident that there was a systematic pixel error in the region 1380 - 1390 nm. This suspicion was confirmed by examining the spectra of the white

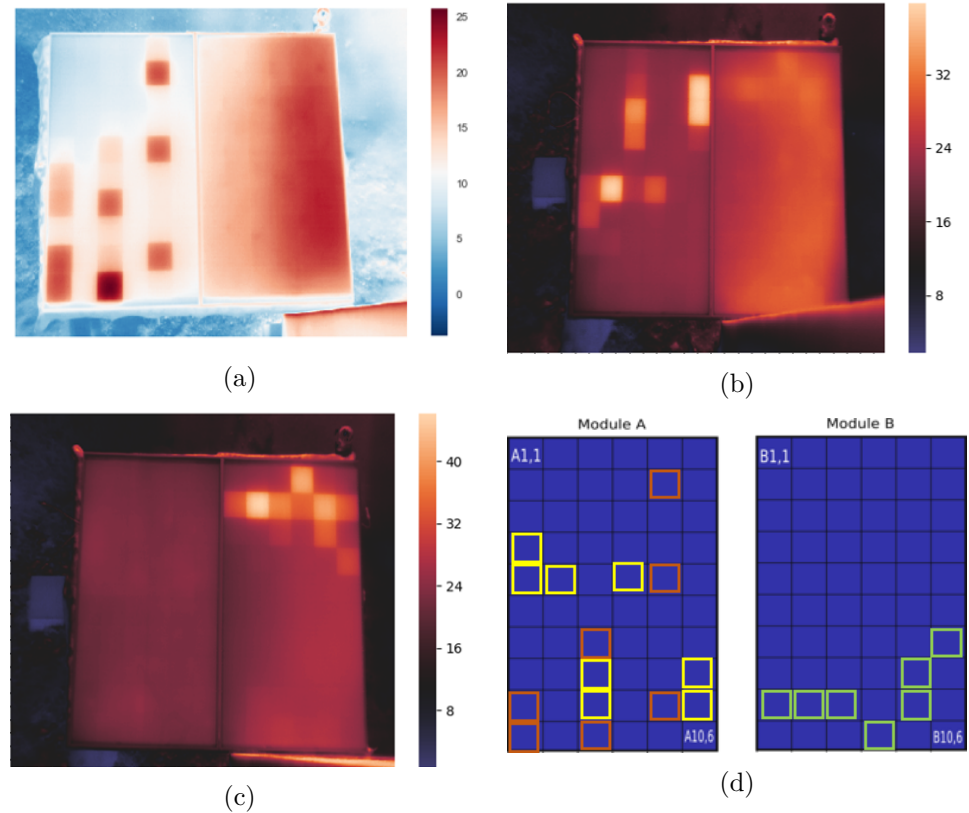


Figure 4.1: IR images taken of module A and B during recordings of HSI. The coloured squares in (d) represent cells from the modules that are clearly overheated in the thermal images. Orange squares corresponds to (a) where module A is in SC and module B is in OC, yellow squares corresponds to (b) where module A is in SC and module B is in OC, green squares corresponds to (c) where module A is in OC and module B is in SC. The colorbars illustrates temperature in °C.

reference during experiment 5 where scans done in a dark room revealed a surprisingly high photon count in that area. This will be commented further in the discussion section, and the results are presented with that information in mind.

4.1 Infrared module inspection

The IR images was primarily used to locate defect cells. When a cell heat up it is because it cannot deliver the same current as the rest of the cells in the same string. In the worst cases all power produced in the string is dissipated as heat in one cell. There can be several reasons for the cell to

4.2. EXCITATION BY LASER AND SOLAR SIMULATOR ON MC-SI CELL33

behave like this, if it is less illuminated than other cells or if there is micro cracks or material defects that increase the resistance in the cell. What is interesting from these results is that the pattern of heated cells of module A is not consistent between 4.1a and 4.1b, which was unexpected. Reasons for the changes in heated cells could be local variations in irradiation, or shadow from nearby buildings or trees which was not noticed during measurements.

This information was used to choose cells to analyse from the HSI. Spectra from *good* cells and *bad* cells were compared, but there was no differences detected so we continued the analysing process using *good* cell because they, in theory, emit more BB radiation.

4.2 Excitation by laser and solar simulator on mc-si cell

Laser excitation

PL images of a mc-Si solar cell taken at room-temperature and 90 K show a significant change in signal intensity between OC and SC conditions. At room-temperature there are areas with high signal in OC shown in 4.2 (a), and in SC they disappear. The PL images at 90 K, figure 4.2 (b) reveals more of the structure in the cell and shows signals at SC that was not visible at room temperature.

Figure 4.3 shows the average spectrum of an area of the cell without busbars. At room-temperature the BB signal peak is the only apparent peak and has a high intensity as shown in figure 4.3a. There is also a big difference in the intensity at BB between OC and SC as seen in figure 4.2.

At 90 K more peaks appear, shown in figure 4.3b. The BB peak is still prominent, but there is also a peak at 0.93 eV and 1.00eV which corresponds with D-lines D3 and D4 respectively. There is also a small elevation in signal around 0.82 eV where D1 is known to be [32]. These are marked with vertical lines in figure 4.3. These results show that it is possible to detect a BB signal in room temperature, but other DRL will not be emitted unless the sample is cooled down.

Solar Simulator excitation

HSI of the cell illuminated by the SS present a barely noticeable difference in signal intensity between OC and SC, but the subtracted spectra, OC-SC, show a large peak in the BB-area. Figure 4.4 shows the HSI of cell 1 in OC (a) and SC (b). It is possible to see a slightly stronger signal in the OC than in the SC image which is confirmed by Figure 4.5 which shows a peak at the BB-area in the subtracted and corrected spectra of the cell. The assumption that DRL signals cannot be recorded in room-temperature is confirmed by these results. Figure 4.5 also shows that there is no peak effects caused by

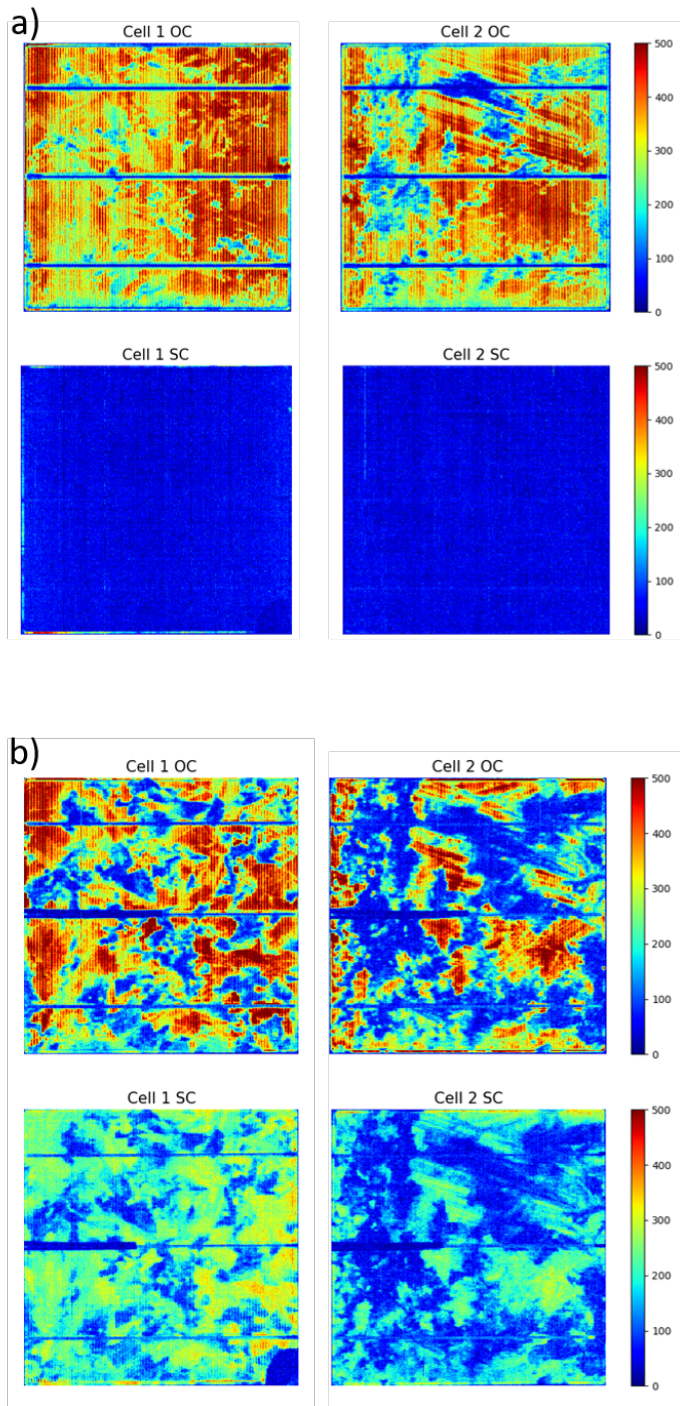


Figure 4.2: PL images of cell1 and cell2 in OC and SC conditions at room temperature (a) and 90 K (b). The colorbars represent signal intensity.

4.2. EXCITATION BY LASER AND SOLAR SIMULATOR ON MC-SI CELL35

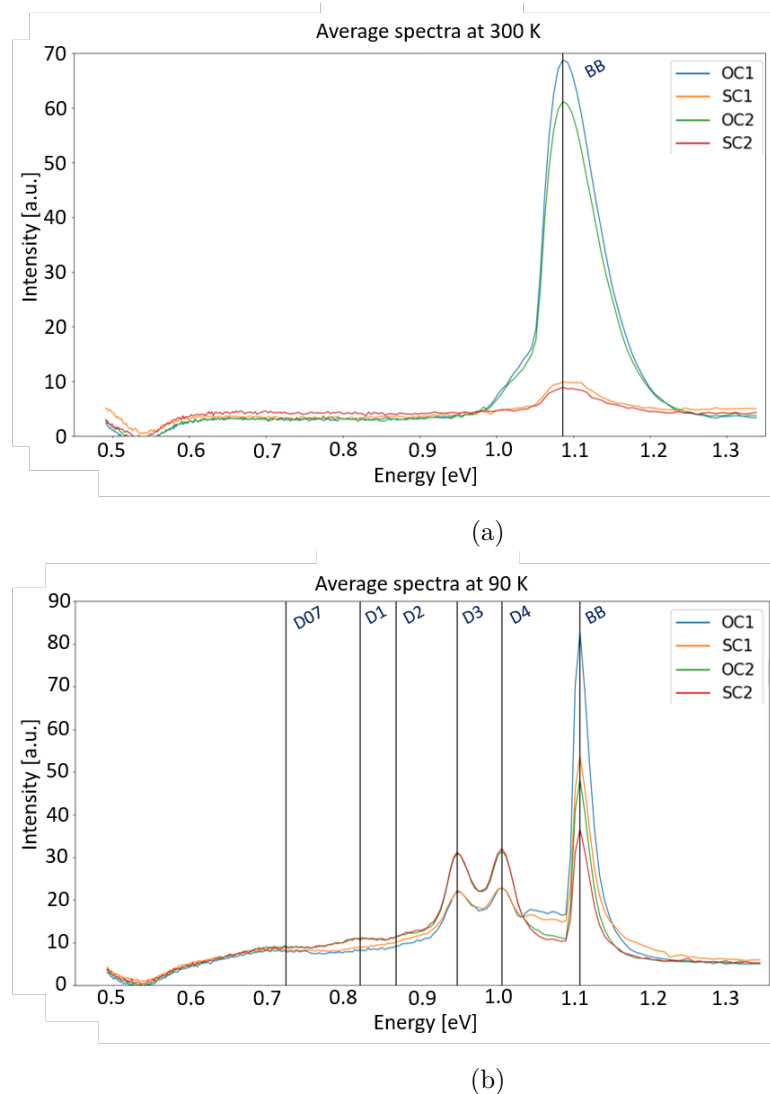


Figure 4.3: PL images in lab of cell illuminated by laser. Images of cell1 and cell2 in OC and SC conditions at room-temperature (a) and 90K (b). In room temperature only the BB signal is visible, but by cooling the sample to 90K DRL luminescence D3, D4 and possibly D1 is visible.

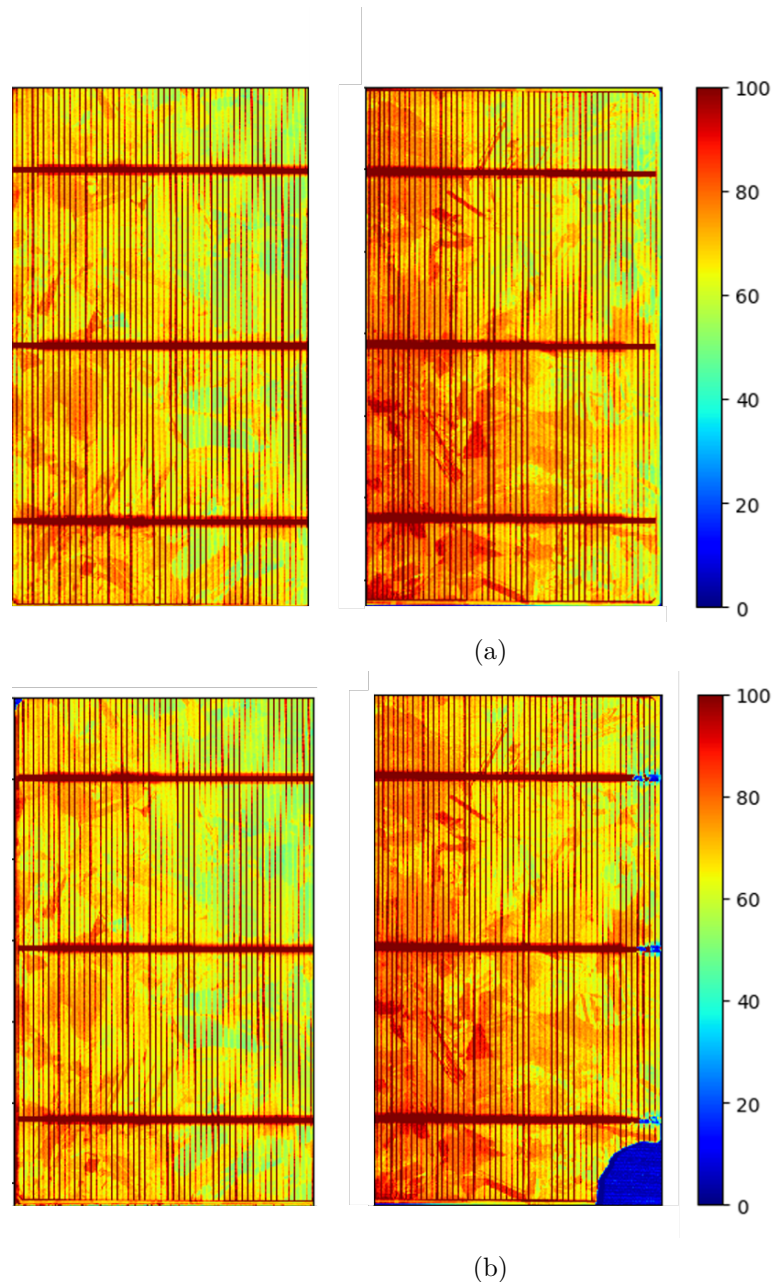


Figure 4.4: PL images in lab of cell 1 illuminated by solar simulator in OC (a) and SC (b). The colorbar represents signal intensity. Pos 1 the HSI to the left and pos 2 is to the right.

4.2. EXCITATION BY LASER AND SOLAR SIMULATOR ON MC-SI CELL37

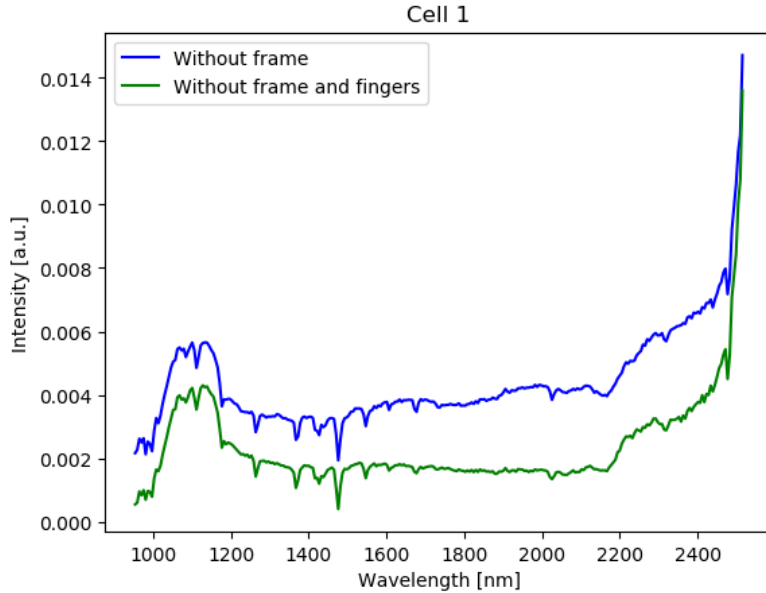


Figure 4.5: Spectra of cell 1 without frame (blue line) and without frame and fingers (green line). There is no change in the spectral characteristic by removing the fingers, but the signal intensity is reduced.

the thin silver contacts coming out from the busbars called "fingers", but the signal strength is uniformly weaker without the fingers. This difference is most likely caused by the removal of cell area close to the fingers during the analysis, and it is known that a large amount of recombination happens in this area.

As expected, the spectral response from the cell under illumination by the SS was a lot weaker than laser excitation. When the cell was illuminated by the SS at 1.0 sun the carrier generation in the illuminated area would be a lot lower than what the laser would generate. However, this difference is not proportional to the difference in intensity. D. Sulas, S. Johnston and D. Jordan [33] showed that surprisingly high scanning laser power densities were needed to reproduce the large area PL. A large area PL at 4 mW/cm^2 compares to a scanning-laser luminescence of 1000 mW/cm^2 , which is attributed to a comparable carrier density per cell after any lateral currents redistribute over the entire cell. When the solar cell was irradiated by the SS the SS was positioned at an angle, which means that the illumination was not uniform across the cell, but stronger closer to the SS. Higher illumination levels will generate more charge carriers, as can be seen on the PL images in figure 4.4 as a higher signal in the area closer to the SS. The spectrum of the SS illuminated cell show a large peak in the BB-area. In

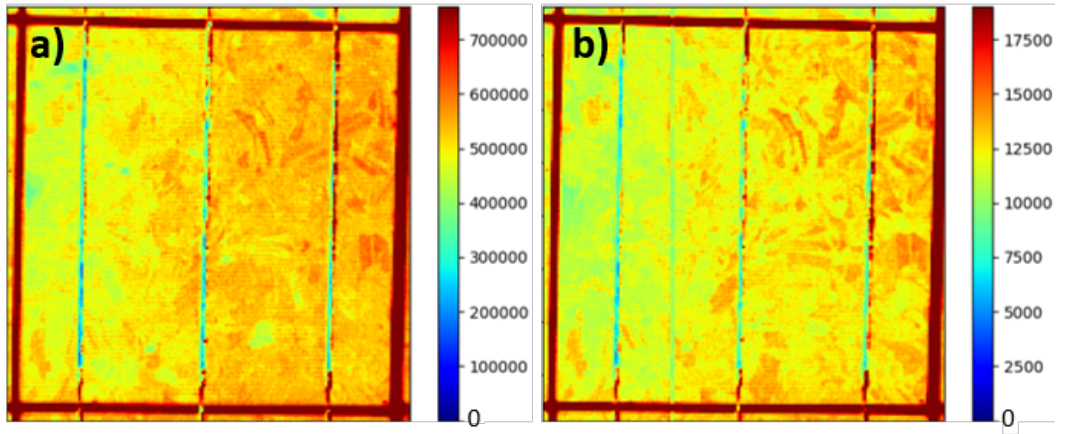


Figure 4.6: Hyperspectral image of cell A8,2 in OC illuminated by solar simulator. a) is integrated over all bands, b) is integrated over bands 30 - 36 (1085-1120 nm). The colorbar represent signal intensity.

the down-right corner of cell 1 in SC a piece of the cell is missing, it broke off after the cell was soldered and cooled down to 90K which makes the material very delicate.

4.3 Luminescence signals from module in lab

Excitation by solar simulator

Results from module A excited with the solar simulator shows a broad and strong peak around 1100 nm from two different cells. Figure 4.7a presents the spectra from WR which fluctuates across the spectra with a slight elevation of signal strength in the area 1000-1050 nm. The white area has a spectra with similar characteristics, shown in figure 4.14b, but has a higher elevated signal in the area between 1000-1200 nm. Figure 4.7c display the spectra of cell A8,2 and a significantly higher signal strength in the BB-area compared to the rest of the spectra. The same characteristics can be seen in figure 4.7d of cell A4,2. The HSI in figure 4.6 shows signal intensity from cell A8,2 for all bands a) and for the BB area b). The HSI images show material structure in the cell, but it is hard to distinguish what is PL signal and what is reflection in 4.6 b), but based on the mean spectra, a considerable part of the signal should originate from PL. These results show that it is possible to detect BB recombination signal with a hyperspectral camera from a PV module illuminated by a spectrum similar to solar irradiation.

A cell outside of the illuminated area was also analysed in this experiment and shows a strong signal in the BB-area. The spectra of cell A10,2 is shown in figure 4.8, which has a very high signal compared to the illuminated cells.

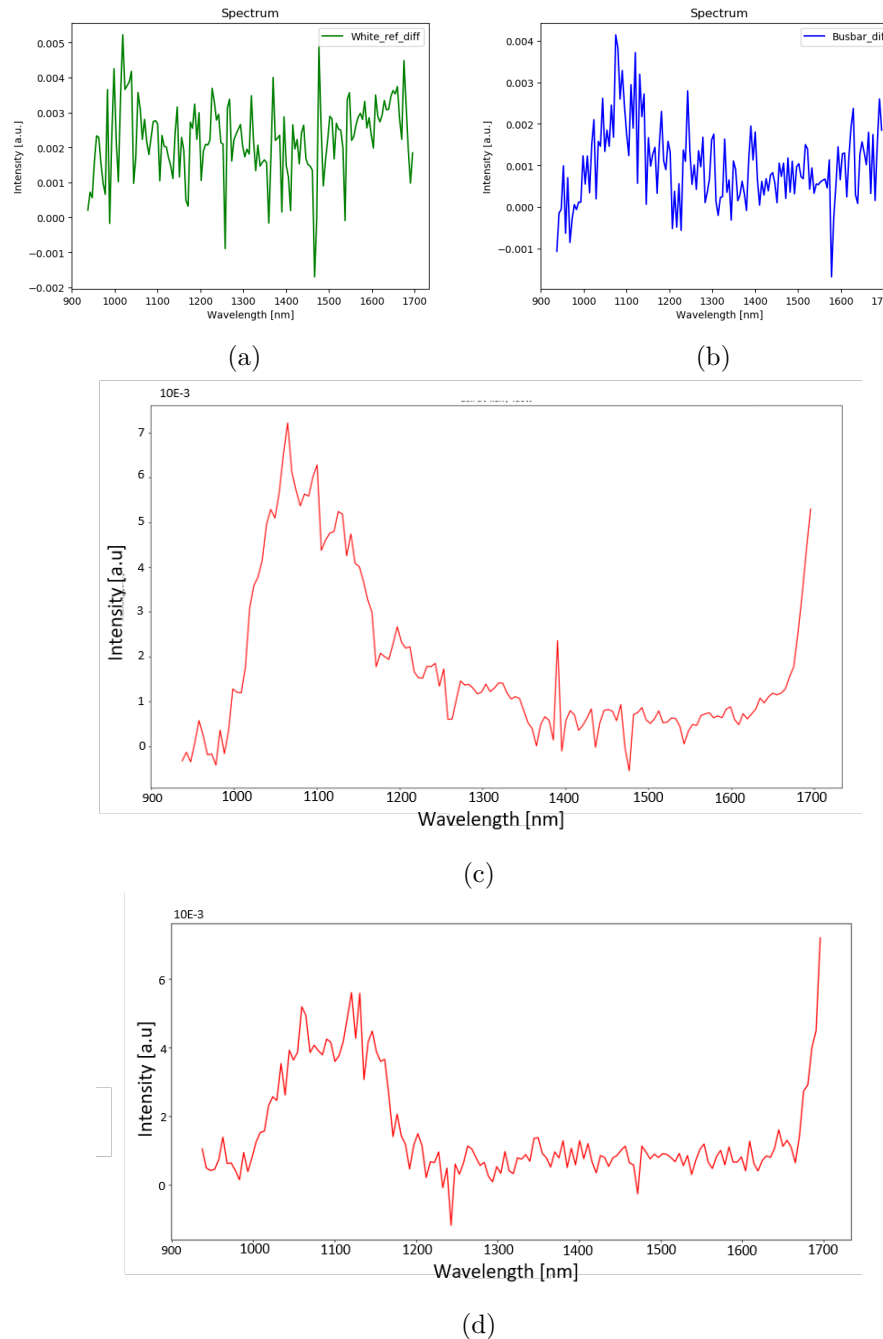


Figure 4.7: Results from experiment 4 displaying spectra of different areas; white reference (a), white area under module glass (b), cell A8,2 (c) and cell A4,2 (d)

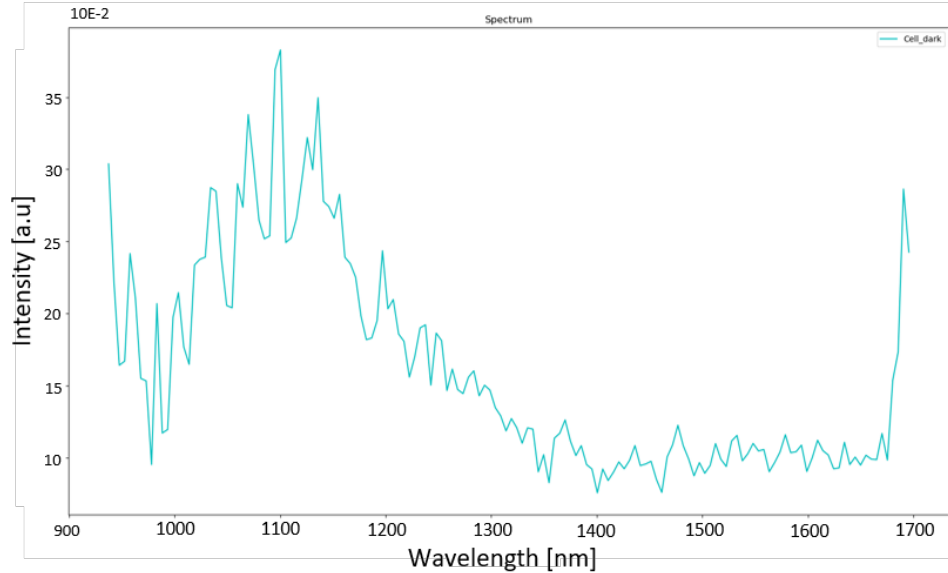


Figure 4.8: Spectra of cell A10,2 situated 2 cells away a cell illuminated by solar simulator. A10.2 exhibit a high signal intensity in the BB area.

Contactless EL is a relatively new technique that combines the versatility of PL imaging with traditional EL and have shown promising results [18] [33]. In these studies a part of a solar cell have been illuminated, and the non-illuminated part has been imaged. In our case it is a whole cell in the same string that have been illuminated, and there have not been published any research of this as we know of. The general form of the spectra resemble that of the illuminated cells, so there is a chance that what we see is diffuse PL signal from the illuminated cells. To know for certain, additional testing is needed. If it is indeed an EL signal that have been recorded, this would be an extremely interesting result to investigate further.

Electroluminescence by external carrier injection

The spectra from 4 different areas of module A connected to an external power source is presented here. Under an applied bias the module emits EL caused by the injected carriers recombining. The images was recorded in a dark room, but the WR was in the camera view to be analysed as a "passive" surface. There is no subtraction done to the spectra due to the fact that under applied forward bias by the current source, the module operates in SC, and is not divided by the WR because there is no illumination in this situation. Figure 4.10 displays the spectra from the WR and the white area between cells. Their characteristics are similar with little noise and a signal at 1350-1500 nm and at 1100-1180 nm. The WR has a strong peak at

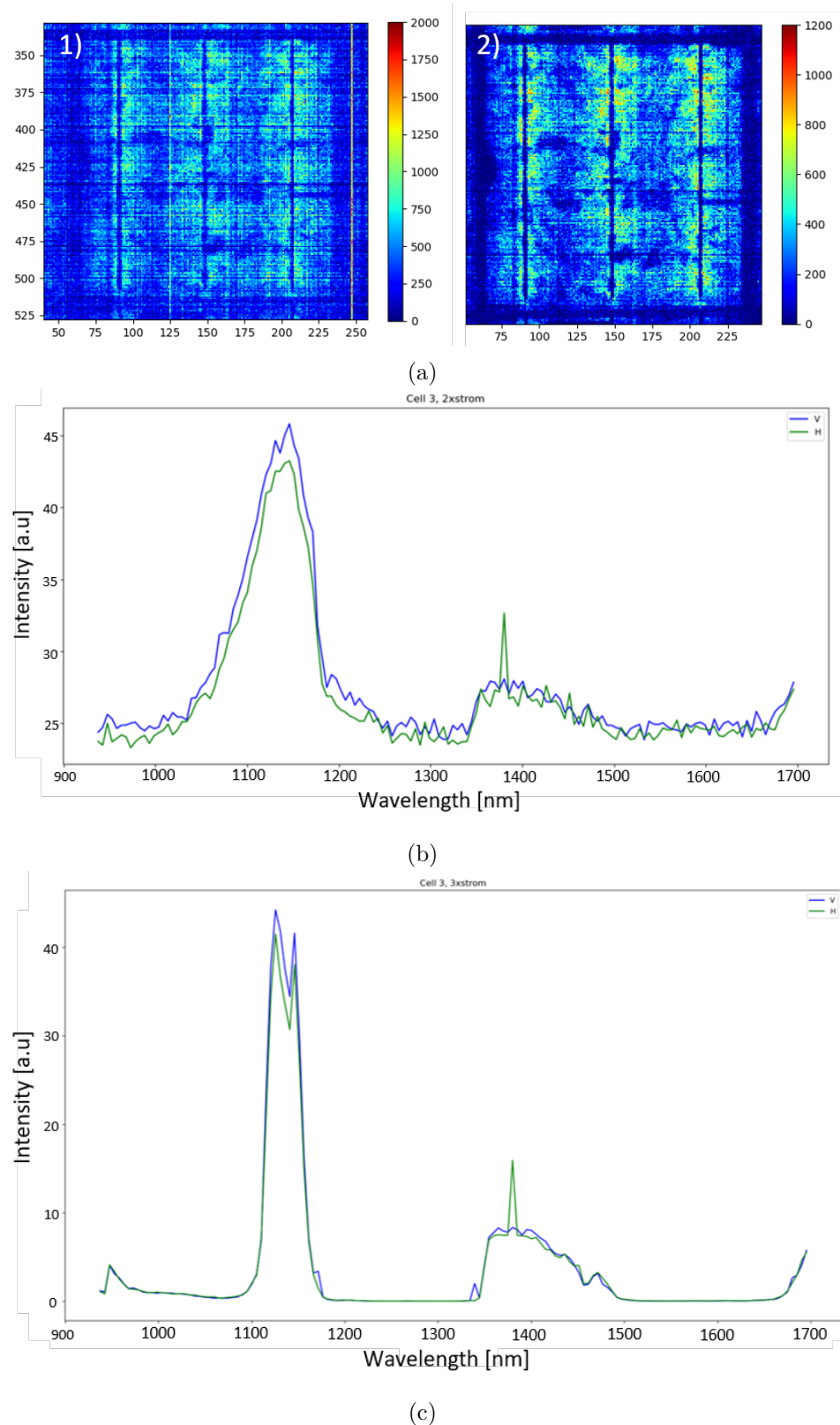


Figure 4.9: Electroluminescence images of cell A8,2 (a), all bands (1), and bands 32-52 (1090-1200 nm) (2). Spectra of the EL signal with a current of 8.06 A and voltage of 1.60 V (b), and current 9.87 A voltage 1.86 V (c).

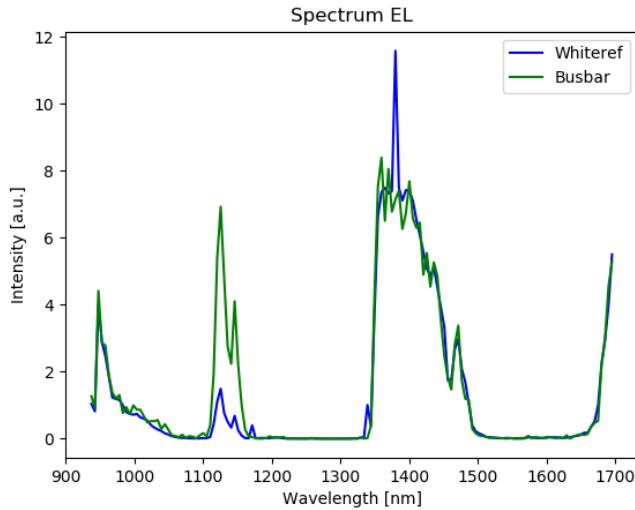


Figure 4.10: Signal from white reference (blue line) and white area between cells (green line).

1380 nm that the white area does not have, and the white area has a much stronger signal in the BB-area.

Two areas of cell A8,2, to the left (blue line) and to the right(green line) of the center busbar, was analyzed and their spectra is presented in figure 4.9c. Their spectra is close to identical, except for a the extra peak at 1380 nm of the blue line. The intensity of the signal at 1350-1500 nm is of the same magnitude as in figure 4.10 but the peak in the BB-area is a lot stronger.

The spatial distribution of signal in figure 4.9a show that there is a higher signal close to the busbars, this characteristic is further enhanced by integrating over bands 32-52 which corresponds to wavelength 1090-1200 nm where the BB signal is expected to be. This shows that the most of the recombination happens close to the busbars with some apparent dark areas with low BB signal which indicates cell defects in said areas.

4.3.1 Detector fault in HySpex SWIR-320i

As mentioned, there are several observations that point in the direction of a detector fault in the HySpex SWIR-320i camera. To investigate this an image taken under EL measurements was integrated over bands 86-90, which covers wavelengths 1375-1396 nm, shown in figure B.3b. To the left in this image a line of strong signal is visible in the y-direction. As the operating principle of a phushbroom scanner is that one pixel-line is acquired at a time, it seems like one pixel in this line have counted a number of photons

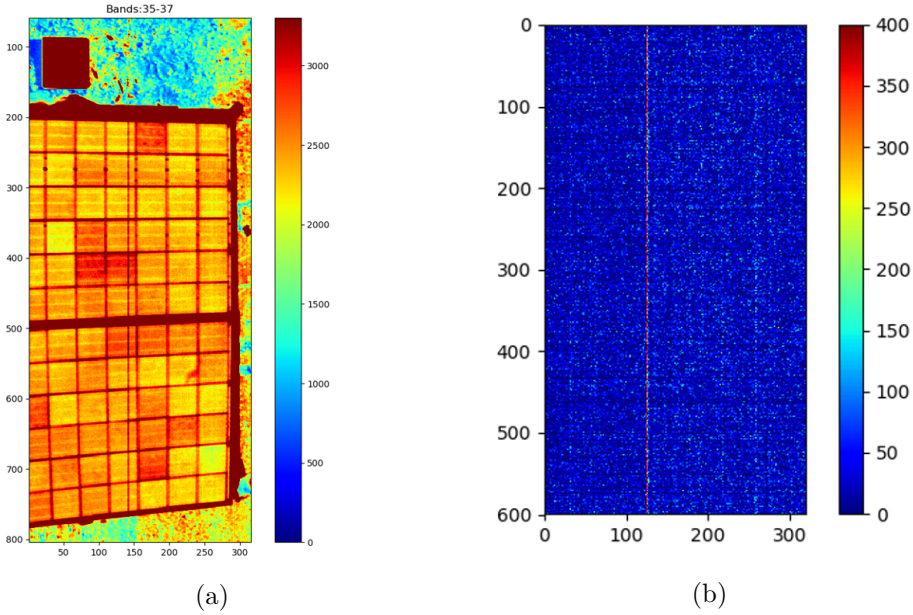


Figure 4.11: Bands 35-37 (1110-1120 nm) of HSI taken in method 3 (a), bands 86-90 (1375-1396 nm) of image taken in dark conditions during EL measurements with HySpec SWIR-320i (b)

that is far greater than the true value. This is the most likely explanation for the prominent peak detected in figure 4.9 blue line (a) and green line (b). In an image taken during data collection at a long distance there is also a line with visibly higher intensity over the module. Image (a) in figure 4.11 which is integrated over bands 35-37 (1110-1120 nm), where we expect to find a BB signal, shows a high intensity line in the middle of the module.

These images confirm the suspicion that there is an error in the HySpec SWIR-320i camera. How much this camera error affects the results are uncertain, but due to the increased signal in the affected areas during outdoor data collection, it could suggest that it is a count error in the detector that is magnified by higher irradiation levels.

4.4 Sunlight excitation in outdoor conditions

This section will present and discuss results from experiments done in outdoor conditions before said results are summarized in a list.

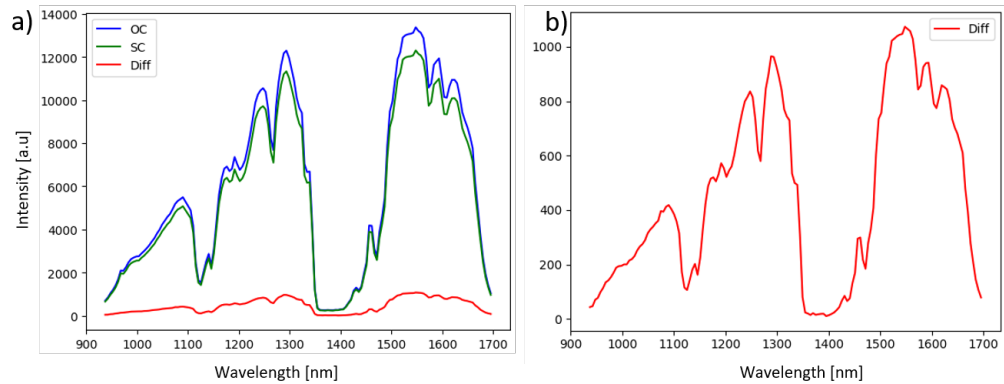


Figure 4.12: Spectral response from experiment 1, test case 1 where the Rig module was imaged in OC and SC. Figure (a) shows the mean spectra of a cell area without busbar in OC (blue line), SC (green line) and the difference between them (red line). The difference in signal is plotted in a smaller scale in figure (b).

4.4.1 HySpex SWIR-i320 recorded images and spectral features

Comparison of same cell in OC and SC with change in illumination

The motivation for this test case was to test the setup and instruments to prepare for the next test. What we learned was that the PL signal is so small that a change in illumination between the image taken in OC and the image taken in SC condition would make the signal disappear all-together. Figure 4.12 shows the difference between OC and SC conditions. The general characteristics resembles the spectrum of global solar radiation as illustrated in figure 2.8. The irradiation levels were between 240 - 280 W/m².

Comparing cells in OC and SC under identical illumination

To eliminate the problem with change in illumination method 2 was designed, where two panels from the same producer was imaged at the same time, one in SC and one in OC conditions. When analysing the images it was clear that the material differences and local reflection from each cell contributed with enough differences that also for this method we were unable to extract the PL signal. Figure 4.13 (a) shows the SC and OC spectra from two different cells A7,5 and B6,3 respectively, and the difference between them (b). As this figure shows, it is too many differences between the cells, like material quality, reflection and diffuse radiation to extract a PL signal. The irradiation varied between 236 W/m² at the start of measurements and 380 W/m² at the end of measurements.

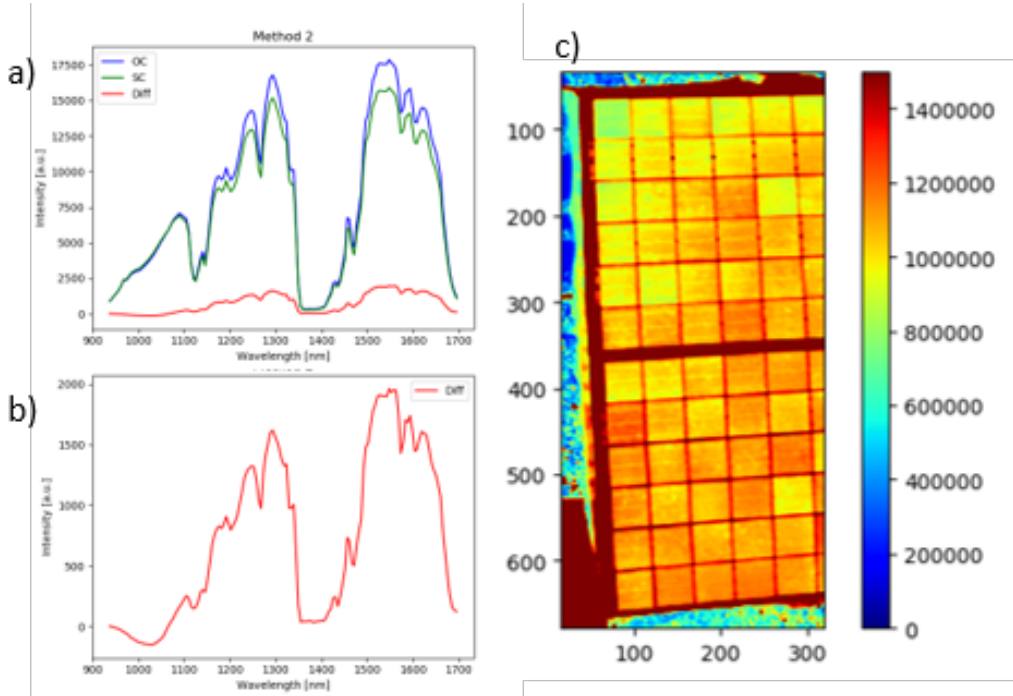


Figure 4.13: Results from method 2 in experiment 3, module A (top) in SC and module B (bottom) in OC. Overview of modules, A in SC, B in OC (a), cell A7,5 in SC and cell B6,3 in OC (b), cell B6,3 in OC subtracted by cell A7,5 in SC (d).

Comparison of same cell in OC and SC by the mean of a series of images

results from this test case shows that the WR is necessary for removing background noise, and by taking the mean of a series of images the effect of changes in irradiation is reduced. During this data collection the irradiation was stable around 600 W/m^2 , but dropped to 570 W/m^2 at the end of the experiment.

Figure 4.14a shows the spectrum of an area of the white reference after it has been corrected by the whole area of the white reference and images taken in OC is subtracted by images taken in SC. The noise is level with fluctuations around -0,001 a.u. photon intensity except for the range from 1350 - 1400 nm where a fluctuation of magnitude 10^{-3} is seen.

A white area under the module glass has the spectral characteristics shown in Figure 4.14b. The spectra of this area deviates from the white reference because of a higher non uniform fluctuation and more prominent peaks. The amplitude of the peak at 1350 - 1400 nm is one order stronger than the for the WR. At 1100-1150 nm there is an elevation in signal intensity in the 10^{-2} range.

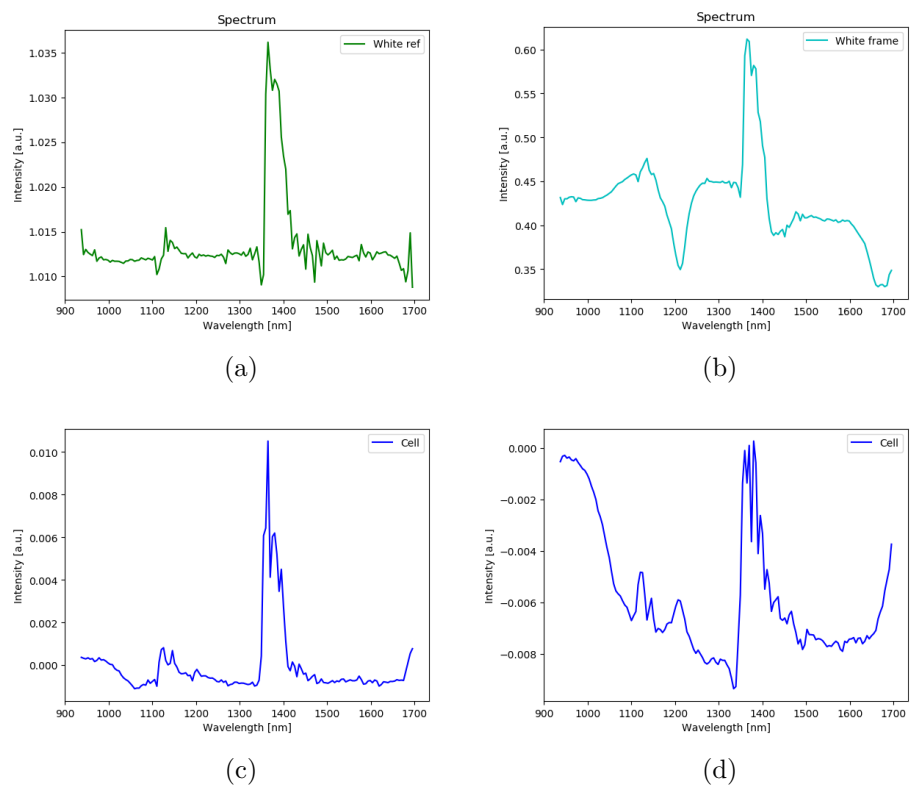


Figure 4.14: Results from experiment 3: Test case 3, displaying signal spectra of different areas; white reference (a), white area under module glass (b), cell A5,3 (c) and cell A3,1 (d)

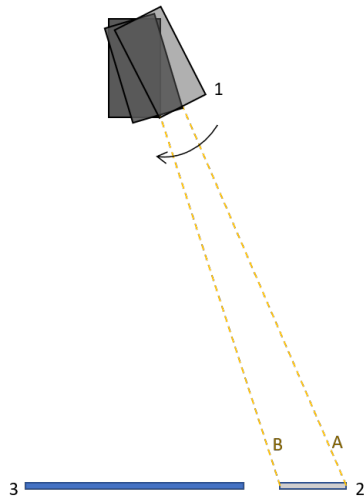


Figure 4.15: Position of camera (1) moving in the direction of the arrow during scans, in relation to the WR (2) and the PV-modules (3). Distance A will be longer than distance B.

Figure 4.14c shows the spectra of cell A5,3 with similar characteristics as the WR. The signal of the peak at 1350 - 1400 nm is one order stronger than the WR, 10^{-2} , and in the BB area there is a signal of magnitude 10^{-3} that do not appear in the WR.

Figure 4.14d shows the spectra of cell A3,1, and has a characteristic that differs slightly from cell A5,3. Overall the signal is weaker with peaks in the BB-area and 1350 - 1400 nm in the 10^{-3} magnitude.

In proportion, the signal from the WR is 1 order larger in the BB region than the general peaks of the signal where SC is subtracted and corrected by the WR. The same applies for the peak at 1400.

Even though the peak in the BB area is smaller than the noise in that area from the WR, the general characteristics differ from the trend in the WR areas. This indicates that there is more than reflection that is measured from the modules.

Inspection of Spectralon plate

The WR was also examined to identify sources of noise, the four corners v1, v2, h1, h2 was corrected with the overall mean of the WR and then plotted together in figure 4.16. This shows that there were some significant differences in reflection within the WR and that it was not homogeneous.

To gain a better control of the uncertainties regarding the WR, 4 different areas were investigated closer. By the same approach as the cells, these areas were analysed and the result is presented in figure 4.14a. Ideally these plots would display a straight horizontal line with a.u. 1, which would mean that

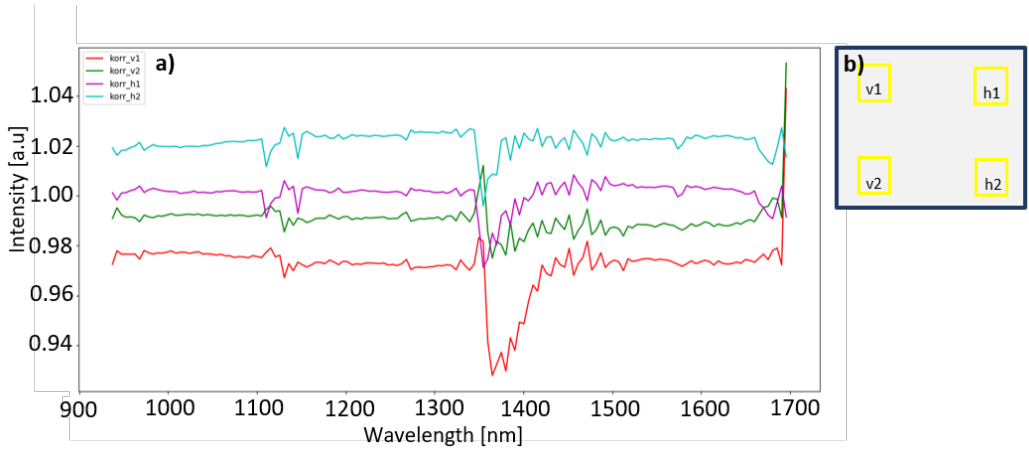


Figure 4.16: Areas v1, v2, h1 and h2 from 4 corners (a) of the spectralon plate used as a white reference in experiment 3. The mean of a series of images for these areas was divided on the mean of the whole solar cell and (b) shows the resulting spectra

the spectral signature of the small area is equal to the spectral signature of the entire WR. Figure 4.14a shows 4 plots, one of each area, that has the same trend, but at different intensities. In other words, the intensity of reflection is not uniform across the WR, and the reflective value at 1100-1150 nm and 1350-1500 nm vary across the WR. The reason for these variations can be due to the angle between the camera and the WR as illustrated in figure 4.15 that cause a difference in the optical path length of the photons, e.g. more photons reach the camera lens from line B than A. Upon visual inspection of the WR it was apparent that area of the plate was soiled and had some areas of discoloration, which could contribute to a non uniform reflection across the plate. More tests are needed to know how big this effect is, but this was not made a priority in this work.

Effects of decreasing distance between camera and module

By changing the distance between camera and sample, the resolution of each cell increases, and possible effects of water vapor absorption decreases. During this data collection, the global irradiance was between 524 and 538 W/m². First the spectra from the WR and a white area is examined before the spectra from two cells are compared with those spectra.

The spectra of the WR in figure 4.17a display a familiar characteristic with low fluctuation except for a prominent peak at 1350-1400 nm, and a small fluctuation in the BB-area. The white area shows more variations in signal, but the same trend can be seen here, with a more prominent signal at BB. The spectra from the white area has the same characteristics but

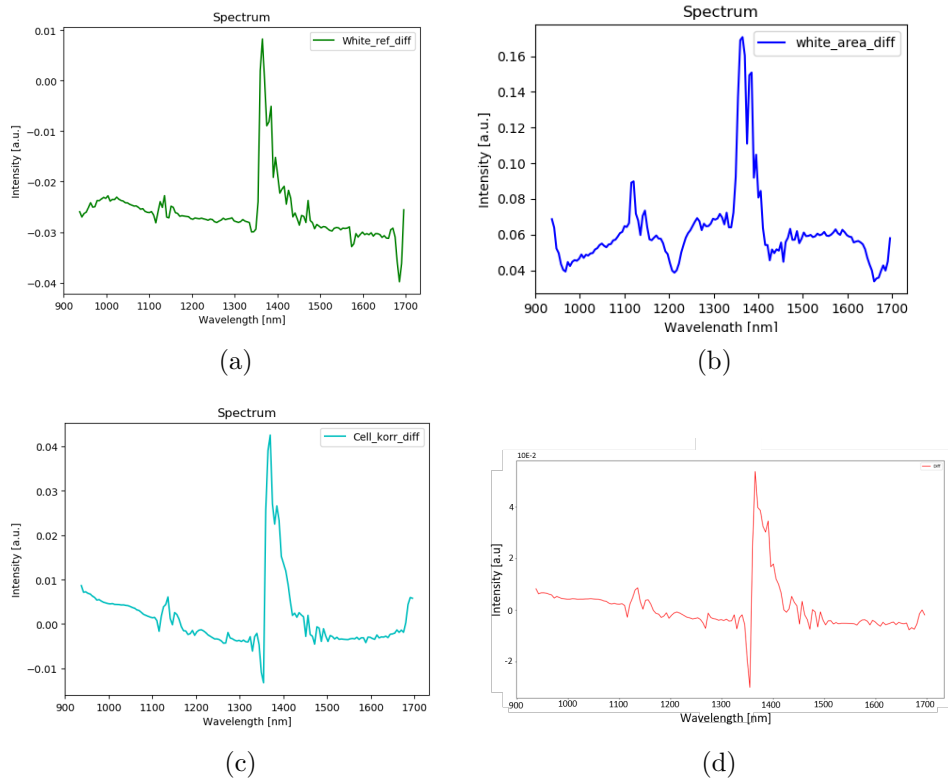


Figure 4.17: Results from experiment 6 displaying spectra of different areas; white reference (a), white area under module glass (b), cell A6,1 (c) and cell A5,1 (d)

slightly stronger signal at both peaks, figure 4.17b.

Figure 4.17c and 4.17d show the spectra of A6,1 and A4,2 respectively. The signal from these cells are close to identical and has the same characteristics as the WR but with slightly stronger signal at both 1350-1400 nm and the BB-area.

To enhance resolution and reduce potential H₂O absorption the camera was placed 1 m from the module for method 3. The area in the frame was therefor reduced to about 3 cells long and almost 2 cells wide. To avoid that the camera shadows any part of the module, it was placed beside the module, straight across from the sun. In this position only the first two columns was in the cameras field of view. To avoid any of the cells going into backward bias because of shade from the WR, a new image was taken with the WR placed on top of the cells after every SC image of cell A6,1 and A5,1. Because cell A8,2 was close to the side of the module, the WR could be placed on the ground next to the module when SC images was taken. The irradiation could have changed between the image of the cells and the

image of the WR, and might contribute to additional noise.

4.4.2 Specim SWIR images and analysis

Detector saturation

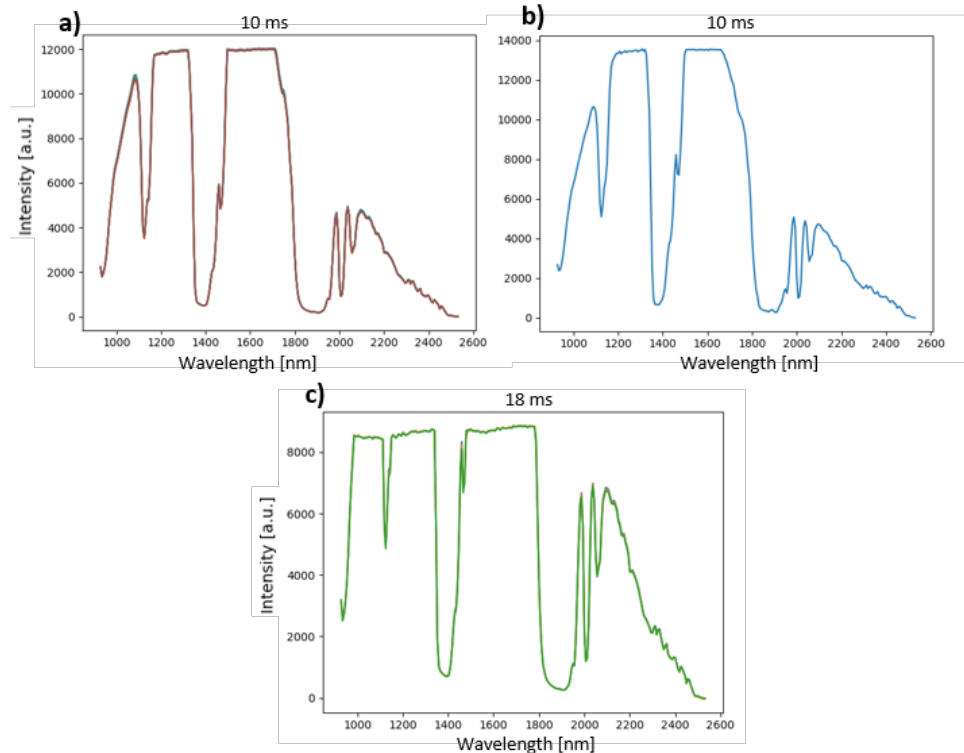


Figure 4.18: Spectral plot of white reference from first data acquisition with Specim SWIR camera with 10 ms integration time (a), second data acquisition with 10ms (b) and 18ms (c) integration time. With 10 ms integration time the detector saturates around 1166 nm and with 18 ms around 900nm.

The spectra from WR images show that the detector got saturated during first and second data collection. During the first data collection the global solar irradiation was between 604 and 618 W/m², and during the second data collection it was between 314 and 455 W/m². Figure 4.18 shows the uncorrected spectra of the WR from the first and second image recordings with the Specim SWIR camera. The detector gets saturated around 1166 nm with 10ms integration time, with 18 ms integration time the detector saturates from 900 nm. This means that the images taken with 18 ms integration time cannot be utilized, but bands up to 1166 nm with 10 ms integration time can be used for analysis.

Spectral characteristics

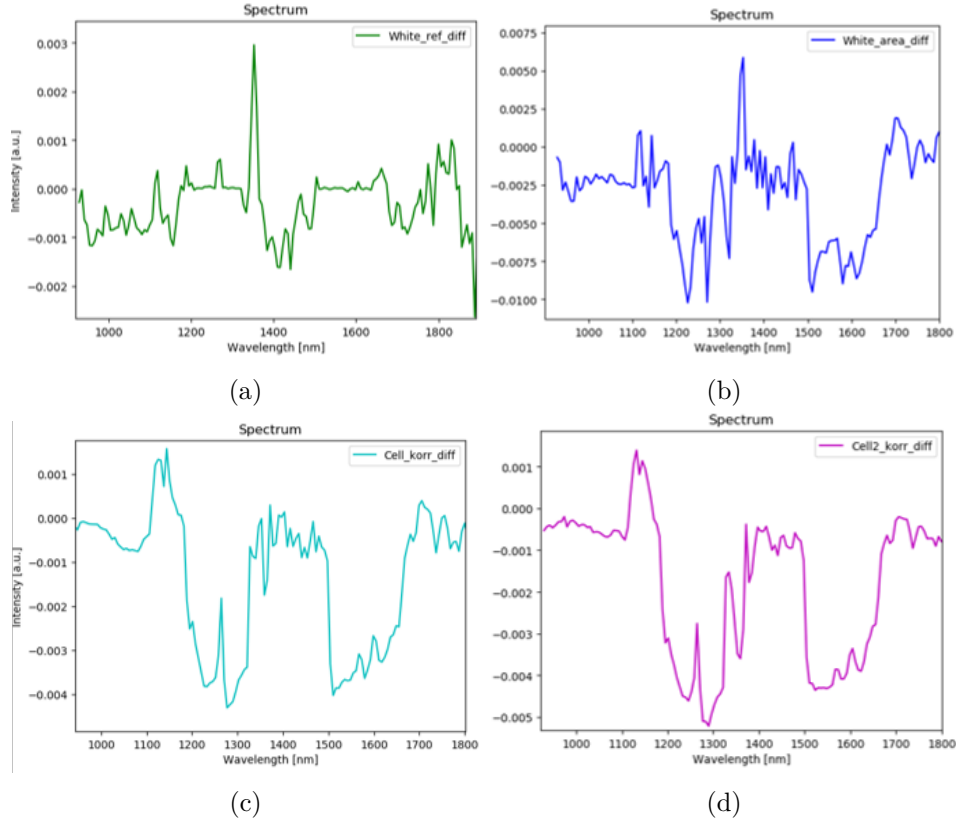


Figure 4.19: Results from experiment 7 displaying spectra of different areas with integration time 10ms; white reference (a), white area under module glass (b), cell A6,1 (c) and cell A5,1 (d)

The Specim SWIR camera was used in the same setup as HySpex SWIR-320i with a distance of 1 m between module and camera. These images reveal a significantly increase in signal intensity in the BB-region. In figure 4.19 results from 4 areas of module A recorded with the Specim camera with an integration time of 10 ms is presented. Because the detector got saturated, the signal above 1160 nm is discarded. The white reference, figure 4.19a display no prominent elevation around the BB-area. The white area in figure 4.19b has a more elevated signal in the BB-area.

The spectra of cell A10,3 shown in Figure 4.19c has a prominent peak compared to the WR in the BB-area, which can also be seen in the spectra of cell A10,4 in figure 4.19d.

Spatial distribution of pixel intensity

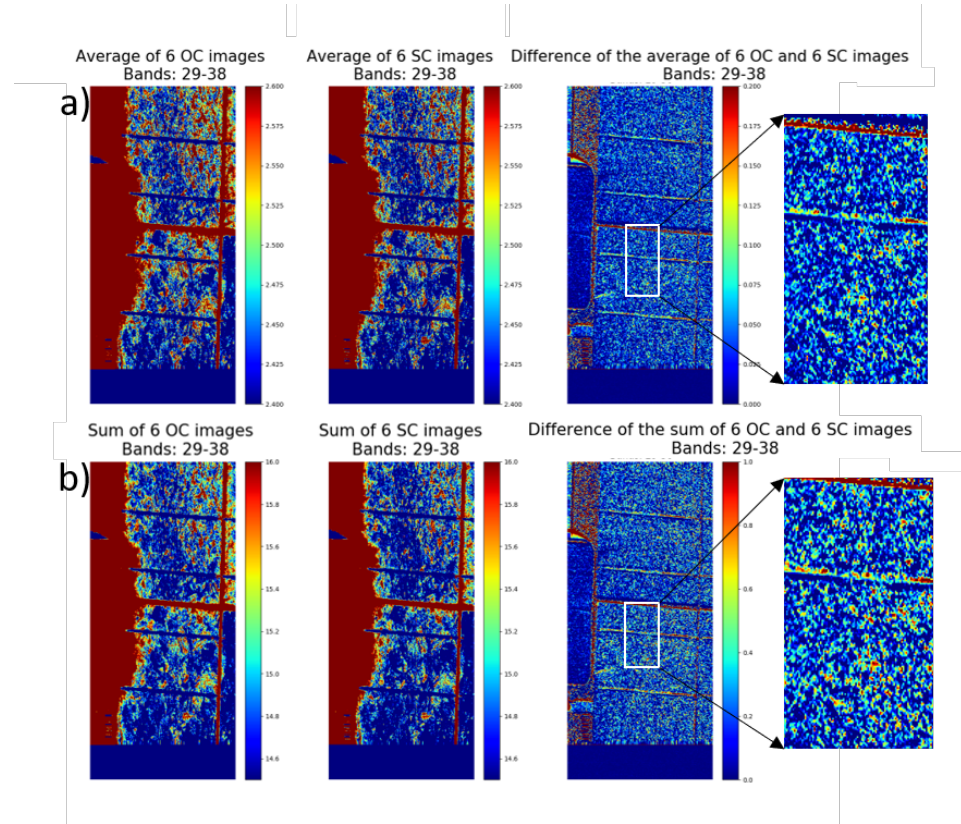


Figure 4.20: Spatial distribution of average of 6 OC images subtracted by the average of 6 SC images (a), and sum of 6 OC images subtracted by the sum of 6 SC images (b), of bands 29-38 which corresponds to wavelength 1079 nm - 1125 nm. The colorbar represents signal intensity.

Results from the previous experiments outdoor indicate that the BB recombination signal is extracted by subtracting SC from OC through examining the mean corrected spectra. This indicates that it is possible to locate the spectral distribution of this signal by subtracting a pixel value in SC from the same pixel in OC. To do this the two images need to have the same dimensions.

6 images from experiment 7 with an integration time of 10ms met the requirement of same dimension. These images were analysed by subtracting the pixel values of one image from another in three configurations, OC-OC and SC- SC as seen in figure 4.22, and OC-SC in figure 4.21. The mean spectra from the three different configurations looks quite similar between OC-OC and SC-SC, but the OC-SC images have a large peak at 1130 nm that cannot be seen in the other configurations. This spectral response can

also be seen by comparing pixel intensities in the HSI images. In the HSI of the OC-SC signal there are some areas that light up more than others, but in general the distribution of high signal pixels looks mostly random. High intensity pixels in this situation means areas where BB recombination occurs more frequently than pixels of lower intensities, e.g. good material quality. More detailed spatial information could be acquired if the resolution had been higher. Another reason for the general randomness in the distribution is the movement when a sample is scanned.

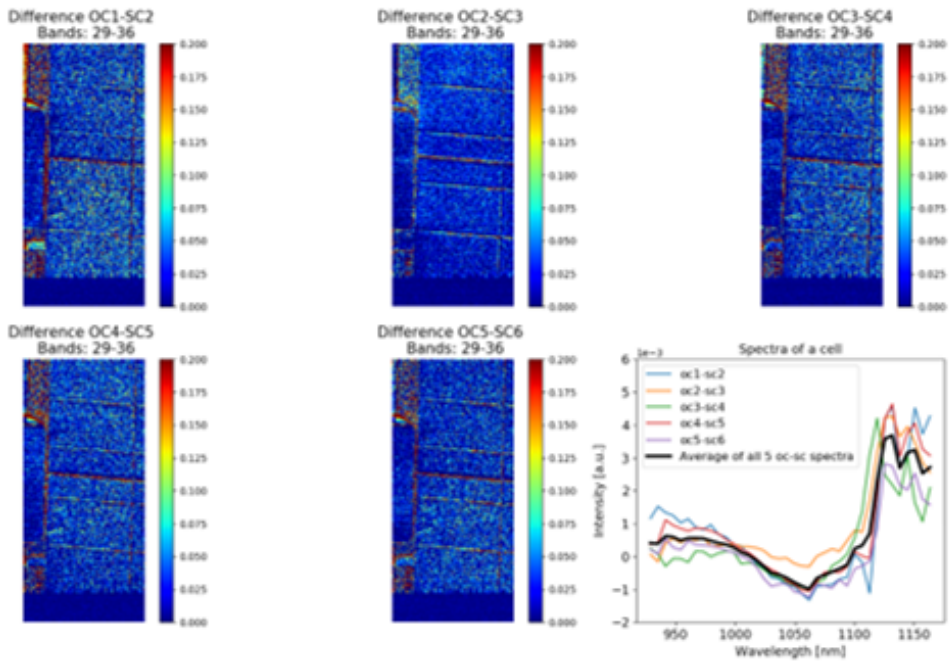


Figure 4.21: 5 OC images are subtracted by 5 SC images. The spatial distribution is showed in HSI where the colorbar indicates signal intensity, while the graph in the bottom right corner show the average spectra of these image configurations.

When the camera scans a sample, either the camera or the sample moves until the appointed number of frames are scanned, before it moves back to its starting position. Even though the frame recording settings are unchanged it often happens that the moving part do not return to the exact same starting position which results in a spatial shift in the x dimension between images. This means that a pixel might get subtracted by a neighbouring pixel in another image which will result in a different value than the true difference. This will contribute to the appearance of a random spatial distribution of signals, but the general result will still be close to the true values.

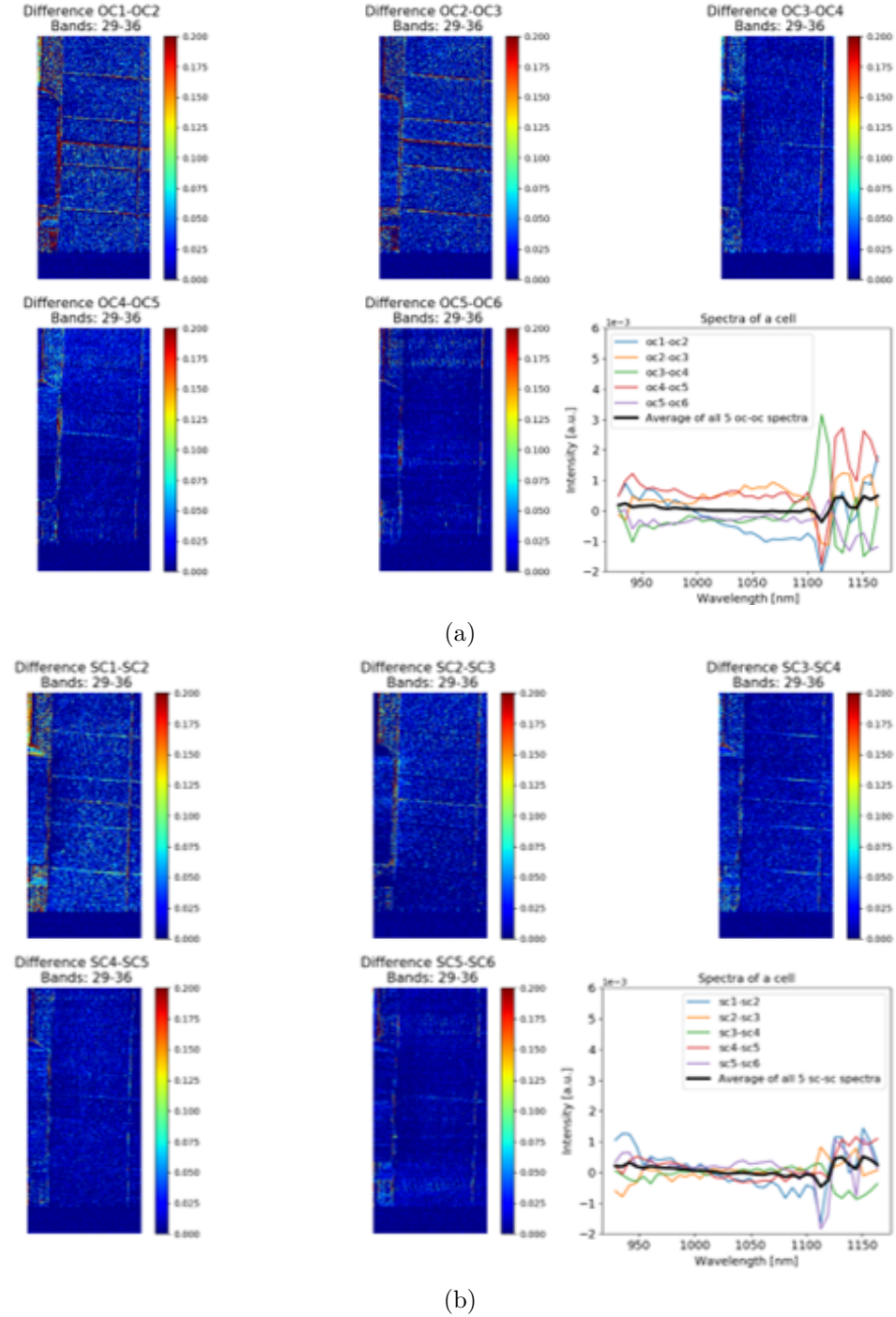


Figure 4.22: 6 images are subtracted with each other in different configurations. The spatial distribution of the remaining signal can be seen in the HSI and average spectra can be seen in the graph. OC-OC images in (a) and SC-SC images in (b)

By taking the average of 6 OC images subtracted by the average of 6 SC images 4.20(a), and sum of 6 OC images subtracted by the sum of 6 SC images (b), we hoped to obtain more spatial detail. In the images of sum and mean of both OC and SC there are areas that light up, but in the subtracted image the signal distribution mostly looks like noise. The magnified area from the subtracted images show some connected pixels with higher signal, and some areas with close to no signal, but there are no areas that can clearly be categorized as *good* areas.

The reason for areas with high signal in the OC and SC images is most likely due to reflection from the material. By subtracting SC values from the OC image, these reflections disappear because they are approximately of the same size. The high intensity area to the left in the OC and SC images is the WR, and appears as a blue rectangle in the difference image.

4.4.3 Summary of section results

Outdoor hyperspectral imaging of photovoltaic modules gave the following results:

- Change in illumination affects results greatly, especially in areas of water absorption and a detector fault were discovered in the HySpex SWIR-i320 camera that contributed to this effect. To remove noise the mean of a series of images taken close in time was divided by a WR under the same illumination before the mean of these was analyzed.
- The corrected images and their OC-SC spectra taken with HySpex SWIR-i320 camera at a distance of ≈ 5 m show a stronger signal from cells in the BB-area than from the WR.
- By changing the distance from 5 m to 1 m the BB signal had the same strength relative to the WR.
- An analyze of the spatial distribution of random signals (OC-OC and SC-SC) compared to expected signals (OC-SC) in two and two images show that there is a significantly stronger signal in OC-SC images. The spatial distribution of high signal pixels reveals regions of high BB light emission as regions with high photovoltaic performance.

4.5 Discussion of results

The experimental work in this thesis opens the possibility for using this technique to detect PL signals from a module outdoor. However, the method needs further improvement before it can be used as a tool for on-site module inspection. PL imaging have been largely limited to single cell measurements because it is a big challenge to design a module-sized uniform light source, therefor it is only in recent years that PL inspections on modules have been conducted.

The results we have gathered makes us positive that we have recorded a signal that comes from PL as a result of BB recombination. Currently these results do not portray enough detail to identify defects in the solar cell, not spectrally nor spatially. The strong signals in the area around 1380 nm is partly due to a detector count error, but it is also likely that small changes in the atmosphere affect the water absorption greatly so that this variation do not get eliminated by taking the average over several images, this will be discussed more thoroughly further down. All things considered, this work shows great promise in the development of a fast, non-destructive way to gather information of module performance in daytime.

4.5.1 Black current and changes in background

To account for the black current, as elaborated in the theory section 2.2, a background image was taken before images of the sample was recorded. The time it takes to collect an image-series vary, but as an example, the image-series taken at long distance outdoor with Spectralon plate 3.4.3, took approx 3 hours from the camera was turned on to the camera was turned off. During this time the sun rose higher and the irradiation grew stronger. A series of 20 OC images was recorded, before a series of 20 SC images was recorded. It is therefore a possibility that increasing temperature of the camera could contribute to changes in the black current density from the first background image was taken to the last SC image was taken. These differences are probably negligible but could contribute to noise.

4.5.2 Integration time

Spectral cameras, unlike traditional trichromatic cameras provide information over a large number of wavelength channels across the electromagnetic spectrum. The image acquisition in this thesis have been done under conditions where the illumination changes, this makes it challenging to produce images with a consistent and reproducible brightness. The goal of this work is to obtain the PL signal emitted from the solar cell material, and the result of incorrect exposure settings, e.g. integration time, may yield dark or overexposed imagery with reduced contrast, which can make the PL signal disappear. There is a trade-off between how long the integration time should be. A higher integration time means more PL signal is recorded, but if any pixels are saturated, we loose control of the signal intensity for that pixel. This is especially challenging when imaging a WR because, as the purpose of using the WR is to reflect as much radiation as possible in the range of the camera detector, the integration time must be adjusted to keep the WR area out of saturation.

4.5.3 Absorption and reflection from module

We know that silicon material has several optical properties, and absorbance and reflectance is different for different parts of the spectrum. When a PV module is illuminated, some of the radiation will be reflected from the module glass, before the remaining radiation either is absorbed, reflected or transmitted through the silicon solar cells. Silicon has high absorption up until the band-gap energy, around 1100 nm. Below this energy level the absorption drops sharply, and at the same time the reflectance increases sharply. These changes have some temperature dependence [34]. As we can see from figure 4.23(c), which is corrected by the WR, there is an increasing signal from 1000 nm. This observation is in accordance with the physical

properties of silicon and the calculations done by *Zhou, Zhang and Ke* in figure 4.23(a) and (b).

4.5.4 Discussion of signal at 1400 nm

As discussed, one of the explanations for the high signal around 1400 nm is due to a camera fault in the HySpex SWIR-320i camera, but some of the same tendencies can be seen in images taken with the Specim SWIR camera. It must therefore be other factors that contribute to the elevated signal.

Effect of iron contaminants

Metal impurities can affect the properties of the solar cell so when discussing the causes of the high signal around 1400 nm that keeps appearing, energy states caused by unwanted impurities was investigated. Iron (Fe_i) is a common impurity and tends to form pairs with substitutional boron (B_s). These Fe_iB_s pairs tend to dissociate into Fe_i and B_s under illumination and most cell parameters tend to degrade during Fe_iB_s dissociation. These pairs create energy levels around $E_c - 0.23 \text{ eV}$ [35], where E_c is the energy of the conduction band in Si, which corresponds to around 0.89eV in the silicon bandgap. 0.89 eV is by the equation 3.1 equal 1393 nm. This means that it is plausible that this effect contributes to the signal at 1400 nm, but this theory is problematic because the spectra of all the WR during outdoor experiments also show a peak in this area which cannot be related to Fe_iB_s pairs.

Effect of water vapor absorption in the atmosphere

As mentioned above, the absorbance decreases, and reflectivity from the module increases around the BB area. This means that a higher signal here is both due to increased PL emissions and high illumination, an additive effect. This area also lies at a dip in the solar spectrum due to water vapor absorption, and we did not know how this would affect the results. What we can see from the spectra of areas from the WR corrected by the WR is peaks wavelengths 1130 nm and 1380 nm, where the peak at 1380 nm have by far the highest signal in the spectrum. These spectra would ideally be a horizontal line with intensity value 1, which means that the reflectance from the small part of the WR is identical to the total area of the WR.

The fact that this signal appears both in images taken with HySpex SWIR-320i and Specim SWIR, means that this most likely an optical property in the reflected signal. This again means that the area divided by the WR has a higher signal intensity in these areas, which point to the fact that during the time it takes to record an image changes in the atmospheric composition affect these areas the most.

It was also uncertainties about what distance between the camera and the sample this absorption would affect the luminescence signal. Images was taken with 1m and 5m distance between the camera and sample, but there is nothing that suggests that this influenced luminescence signal. This is probably a bigger problem in remote sensing where distances between scene and camera is far greater.

One way to gain better understanding of this absorption effect would be to compare images taken indoor with images taken outdoor. The spectra from the solar simulator used here can be seen in figure 3.7 and it is evident that this spectrum looks nothing like the solar spectra, and for these images it does not make sense to compare absorption effects.

4.5.5 Comparison with similar study

A related study to our proposed method is *Outdoor photoluminescence imaging of photovoltaic modules with sunlight excitation* [7]. In Boopathy *et al.*, work they used a hyperspectral camera to image PV modules outdoor and to extract the BB radiated signal from specular diffuse radiation they periodically modulated the PL emission by changing the operating point of the cells using a LED lamp to switch the imaged string from OC to SC condition. They did not use a WR to correct for reflected signals, but a band-pass filter with cut-on and cut-off wavelengths of 1125 nm and 1150 nm that was mounted on the camera. The way they extracted the PL signal is therefor quite different from our technique. Their results revealed various electronic defects in a PV module through high quality PL images. But they had a big confidence that the signal obtained by subtracting SC from OC spectra was the PL signal. Experience from this thesis points in another direction, where changes in illumination between acquiring OC and SC images affects the small difference between the PL signal in these conditions in an extent that drowns the signal in noise. In Bhoopathys article, [7], they also point out that it is beneficial that the luminescence emission peak from crystalline silicon coincides with the dip in of the solar spectrum due to water absorption. Due to the low radiation in this area it is beneficial, but as our discoveries point out, small changes in the atmosphere affects this part of the spectrum in a large degree, which was one of the reasons why we saw the need to correct every image with the reflection from a WR. But even though these two studies have some different interpretations of challenges with this method, both point to the conclusion that there is great potential in this method of studying cells or modules under normal operation in the field.

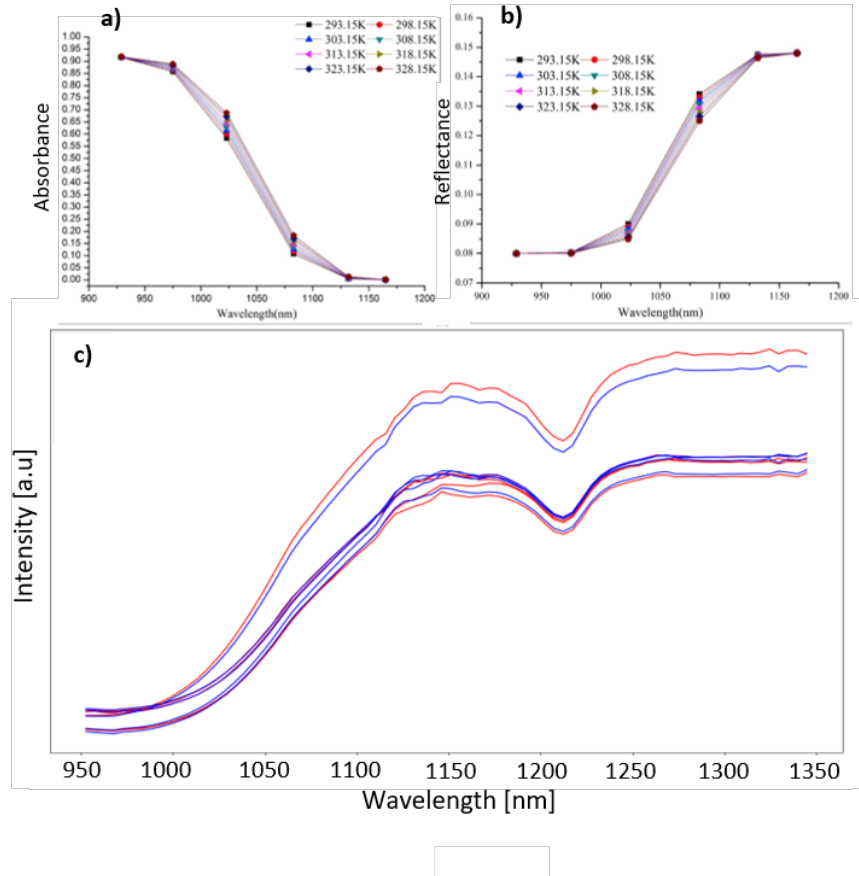


Figure 4.23: Absorption and reflection in silicon solar cells. Figure a) shows absorbance properties in Si, it has its maximum at 920 nm and minimum at 1150 nm, figure b) shows reflective properties in silicon which has a minimum at 950 nm and maximum at 1150 nm, with small variations with temperature. Figure c) shows OC signal corrected by WR for cells in Module A which displays these optical properties.

Chapter 5

Conclusions

The main goal of this research has been to explore the method of hyperspectral PL imaging of solar cells, and to answer the research question if hyperspectral imaging can be used to investigate degradation in solar cells. We have proven that the PL signal is possible to detect both in laboratory by excitation with photons and current injection, and outdoor. The indoor measurements yielded good results, and the BB peak was visible when a mc-Si solar cell was illuminated by a line laser of 808 nm and by a solar simulator. A commercial mc-Si PV module with 60 solar cells in 3 strings was also imaged in the lab when illuminated by a solar simulator and by carrier injection through an external current source. These tests also yielded a strong signal in the BB area. The results from illuminating the module with a solar simulator showed that it is possible to detect a PL signal from a module with solar irradiation. To further explore the method the instruments were taken outdoor to image a module in daylight under normal operating conditions, which to the extent of our knowledge is the first time a hyperspectral camera with a white reference has been used to image modules in daylight. The outdoor image acquisition was done with several variations with two different cameras, which yielded various results. The following list summarizes the most important findings of the presented work.

- Excitation of mc-si solar cells by laser and solar simulator yield a strong PL signal in the BB-area
- By cooling the cell to 90 K, DRL corresponding to D-lines D3 and D4 was visible in addition to a BB signal
- By illuminating a module with a solar simulator, a prominent and broad peak in the BB area was visible, which confirmed that it is possible to measure PL signals from a module by solar excitation
- Imaging of EL with external carrier injection via contacts and illumination by solar simulator yielded PL signals but with distinct differences

between the PL and EL spectral characteristics.

- By taking the mean of a series images of a module illuminated by daylight in OC and SC suggested a peak in BB area but a low signal to noise ratio posed a problem in deciding if this was really a PL signal. A different camera was used in the same setup and yielded a stronger signal in the same wavelength area.

To increase the certainty that it is indeed the PL signal that we have extracted, several measures were taken. A white reference (Spectralon) was introduced to account for specular reflection. The mean values of a series of images that was taken over a short time interval, was used to account for changes in illumination. By subtracting the image of a cell area in SC from an image of the same cell area in OC the remaining signal is assumed to be a PL signal. During lab tests this signal was strong when a module was illuminated by a solar simulator, but during the first experiments outdoor, this signal was barely visible and not distinguishable from noise. Several new experiments were performed with the HySpex SWIR-320i, and by changing camera to Specim SWIR the peak in BB-area around 1120 nm was more prominent than from the HySpex camera. The promising results from the Specim camera lead to further analysis of the images. By looking at two and two of the images the average difference between OC and SC images showed a peak in the BB-area that could not be seen by subtracting OC with OC images or the SC with SC images. This further substantiate the use of this method for PL imaging. An important part of this research was to establish how this technique could be used in further research on degradation in solar cells, and if it has promise of being utilized for industry purposes. Consequently the spatial distribution of PL signal was important to investigate. By the same approach as looking at spectra of two and two images, the spatial distribution of signal from OC subtracted by OC, SC from SC and SC from OC was inspected, figure 4.22a, figure 4.22b and figure 4.21 respectively. From this analysis there seemed to be more signal from the OC-SC images in general, but the high intensity pixels were scattered all over the cells without revealing any *good* or *bad* areas in the cell. To see if more details could be extracted, the average and sum of the images was presented in figure 4.20. These images show some high signal areas in both average and sum of OC and SC images, but the OC-SC images still portray a signal distribution that resembles noise, but with slightly more detail than in figure 4.21. By magnifying an area of the image, some connected lines with high intensity pixels can be seen. The expectations from these images was that more restricted areas in the cell would light up to indicate where most of the BB recombination happens. The reason that the expectations was not met could be several. One is that for each of these images the camera physically moves on a linear translation stage, which

sometimes leads to a spatial shift in the images because the camera starts the recording at a slightly different position between some of the scans. Changes in diffuse reflection between images that is not removed by the white reference correction could be another reason. A stronger signal could have been achieved by increasing the integration time. This way more PL photons will reach the detector during scans, the problem with increasing the integration time is that the detector is more easily saturated by specular reflection from the WR.

Due to the consistency in measurements that point in the direction of an extracted PL signal I am confident that this technique is working. There is still a lot to be done, in both improving the method and to verify it, but the potential is great

The experiments have mostly been exploratory, which have resulted in some weaknesses in the way the tests have been performed and how the data have been processed. In the experimental setting there was no measurements of voltage and current generation in the module during image acquisition, which would have been helpful to predict the strength of PL signal, and if the experiments were to be recreated. When images were recorded at a distance of 1 m we did not have any solar irradiation measurement equipment. The irradiation data comes from a weather station connected to the university 850 m away from where the module was placed, which means that we do not have full control of the amount of radiation the module experienced. The module was also carried around between experiments, and it is a possibility that it can have experienced damages like micro cracks or more severe contact damages. This would affect the carrier generation and diffusion length which again could reduce the emitted PL signal between experiments.

So far the method is not accurate enough to be used for monitoring degradation, but I strongly believe that the advancements of experimental design that has come from this work prove that the method can, after further improvement, eventually be used for that purpose.

Further work

Following the work on this thesis the main focus should be improving the method. This involves getting control of all reflections both specular and diffuse and know the effect of this. Use filter and a camera that covers a smaller spectral area, mainly the wavelengths from 1100 nm to 1200 nm. And find the optimal integration time and irradiation conditions to conduct measurements.

In addition to these improvements, two studies should be done:

- Take images as before, but take pairs of OC and SC images in close succession. Build up a big data set and try out different algorithms and statistical methods and see if the BB signal can be identified.
- Explore the method of contactless electroluminescence. This method, if it can supply enough detail, has many practical advantages, and can be a candidate to use in remote sensing by placing the setup in a drone to further increase its utility

Silverman et al. [6] collected 2000 images, 1000 OC and 1000 SC, to reach a satisfying level of detail in their results. With such a large data set, new possibilities for data analysis open.

Bibliography

- [1] D. Jordan and S. Kurtz, “Photovoltaic degradation rates - an analytical review.” *Progress in Photovoltaics: Research and Applications*, June 2012.
- [2] REN21, *Renewables 2018. Global Status Report*, 2018.
- [3] I. E. A. Secretariat, *Renewables 2018, Analysis and forecasts to 2023, Executive Summary*. Market Report Series, 2018.
- [4] J. Giesecke, M. Schubert, B. Michl, F. Schindler, and W. Warta, “Minority carrier lifetime imaging of silicon wafers calibrated by quasi-steady-state photoluminescence,” *Solar Energy Materials and Solar Cells*, vol. 95, no. 3, pp. 1011 – 1018, 2011.
- [5] A. Datta, M. Song, J. Wang, M. Labrune, S. Chakroborty, P. R. i Cabarrocas, and P. Chatterjee, “Photoluminescence spectrum from heterojunction with intrinsic thin layer solar cells: An efficient tool for estimating wafer surface defects,” *Journal of Non-Crystalline Solids*, vol. 358, no. 17, pp. 2241 – 2244, 2012. Proceedings of the 24th International Conference on Amorphous and Nanocrystalline Semiconductors (ICANS 24) Nara, Japan August 21-26, 2011.
- [6] T. J. Silverman, M. G. Deceglie, K. VanSant, S. Johnston, and I. Re-pins, “Illuminated outdoor luminescence imaging of photovoltaic modules,” in *2017 IEEE 44th Photovoltaic Specialist Conference (PVSC)*, pp. 3452–3455, June 2017.
- [7] R. Bhoopathy, O. Kunz, M. Juhl, T. Trupke, and Z. Hameiri, “Outdoor photoluminescence imaging of photovoltaic modules with sunlight excitation,” *Progress in Photovoltaics: Research and Applications*, vol. 26, no. 1, pp. 69–73, 2017.
- [8] W. Shockley and H. J. Queisser, “Detailed balance limit of efficiency of p-n junction solar cells,” *Journal of Applied Physics*, vol. 32, no. 3, pp. 510–519, 1961.

- [9] V. Alex, S. Finkbeiner, and J. Weber, “Temperature dependence of the indirect energy gap in crystalline silicon,” *Journal of Applied Physics*, vol. 79, no. 9, pp. 6943–6946, 1996.
- [10] D. W. Rankin, “CRC handbook of chemistry and physics, 89th edition, edited by David R. Lide,” *Crystallography Reviews*, vol. 15, no. 3, pp. 223–224, 2009.
- [11] R. T. Fonash and S. Ashok, “Solar cell.” <https://www.britannica.com/technology/solar-cell>, September 2018. Accessed: 2019-01-12.
- [12] PVEducation, “PN-junction - Doping.” <https://www.pveducation.org/pvcdrm/pn-junctions/doping>. Accessed: 2019-05-26.
- [13] B. Van Zeghbroeck, *Principles of semiconductor devices*. University of Colorado, 2011.
- [14] O. Breitenstein, F. Frühauf, J. Bauer, F. Schindler, and B. Michl, “Local Solar Cell Efficiency Analysis Performed by Injection-dependent PL Imaging and voltage-dependent lock-in thermography,” *Energy Procedia*, vol. 92, pp. 10 – 15, 2016. Proceedings of the 6th International Conference on Crystalline Silicon Photovoltaics.
- [15] A. Wincukiewicz, W. Mech, S. Grankowska, W. Agnieszka, A. Draibińska, T. Slupinski, K. Korona, and M. Kaminska, “Radiative recombination and other processes related to excess charge carriers, decisive for efficient performance of electronic devices,” *Lithuanian Journal of Physics*, vol. 58, 03 2018.
- [16] A. Smets, K. Jäger, O. Isabella, R. Van Swaaij, and M. Zeman, *Solar Energy - The physics and engineering of photovoltaic conversion, technologies and systems*. 02 2016.
- [17] G. M. Wyller, “Correlation of defect luminescence and recombination in multicrystalline silicon,” master thesis, Norwegian University of Life Sciences Faculty of Science and Technology, 2015.
- [18] S. Johnston, “Contactless electroluminescence imaging for cell and module characterization,” in *2015 IEEE 42th Photovoltaic Specialist Conference (PVSC)*, pp. 1–6, June 2015.
- [19] S. Pizzini, M. Guzzi, E. Grilli, and G. Borionetti, “Photoluminescence emission in the 0.7-0.9 eV range from oxygen precipitates, thermal donors and dislocations in silicon,” *Journal of Physics: Condensed Matter*, vol. 12, p. 10131, November 2000.
- [20] E. Olsen, S. Bergan, T. Mehl, I. Burud, K. Ekstrøm, and M. Di Sabatino, “Defect related radiative recombination in mono-like

- crystalline silicon wafers," *physica status solidi (a)*, vol. 214, no. 8, p. 1700124, 2017.
- [21] A. Flø, I. Burud, K. Kvaal, R. Søndenå, and E. Olsen, "Distribution of radiative crystal imperfections through a silicon ingot," *AIP Advances*, vol. 3, November 2016.
 - [22] D. Wu and D. Sun, "Advanced applications of hyperspectral imaging technology for food quality and safety analysis and assessment: A review à part i: Fundamentals," *Innovative Food Science and Emerging Technologies*, vol. 19, pp. 1 – 14, 2013.
 - [23] J. Burger and A. Gowen, "Data handling in hyperspectral image analysis," *Chemometrics and Intelligent Laboratory Systems*, vol. 108, no. 1, pp. 13 – 22, 2011. Illustrations reprinted with permission from Elsevier.
 - [24] S. I. Imaging, "Ccd read noise dark current." <https://specimg.com/technology/ccd-read-noise-and-dark-current/>, note = Accessed: 2019-05-26,,
 - [25] K. Dornelles, M. Roriz, V. Roriz, and R. Caram, "Thermal performance of white solar-reflective paints for cool roofs and the influence on the thermal comfort and building energy use in hot climates," August 2011.
 - [26] C. Fröhlich, "Solar constant and total solar irradiance variations." Encyclopedia Sustainability, May 2010.
 - [27] M. A. Green and M. J. Keevers, "Optical properties of intrinsic silicon at 300 k," *Progress in Photovoltaics: Research and Applications*, vol. 3, no. 3, pp. 189–192.
 - [28] B. Swatowska, T. Stapiński, K. Drabczyk, and P. Panek, "The role of antireflection coatings in silicon solar cells - The influence on their electrical parameters," *Optica Applicata*, vol. XLI, p. 487, January 2011.
 - [29] N. E. Solutions, "Solar cell solar panel difference." <https://www.novergysolar.com/solar-cell-solar-panel-difference/>. Accessed: 2019-05-16.
 - [30] D. C. Miller, J. Bengoechea, J. Bokria, M. Koehl, N. E. Powell, M. E. Smith, M. D. White, H. R. Wilson, and J. H. Wohlgemuth
 - [31] R. Kroon, "Reflection measurements for luminescent powders," *Physica B: Condensed Matter*, vol. 535, pp. 181 – 183, 2018. 7th South African Conference on Photonic Materials SACPM 2017.
 - [32] T. Mehl, *Hyperspectral Photoluminescence Imaging of Silicon Wafers and Solar Cells*. PhD dissertation, Norwegian University of Life Sciences Faculty of Science and Technology, 2018.

- [33] D. B. Sulas, S. Johnston, and D. C. Jordan, “Comparison of photovoltaic module luminescence imaging techniques: Assessing the influence of lateral currents in high-efficiency device structures,” *Solar Energy Materials and Solar Cells*, vol. 192, pp. 81 – 87, 2019.
- [34] J. Zhou, Z. Zhang, and H. Ke, “Pv module temperature distribution with a novel segmented solar cell absorbance model,” *Renewable Energy*, vol. 134, pp. 1071 – 1080, 2019.
- [35] J. Schmidt, “Effect of dissociation of iron boron pairs in crystalline silicon on solar cell properties,” *Progress in Photovoltaics: Research and Applications*, vol. 13, no. 4, pp. 325–331.

Appendices

Appendix A

Python script for HSI processing

A.1 Example code for data processing

```

1 # -*- coding: utf-8 -*-
2 """
3 Created on Sat May 18 13:46:10 2019
4
5 @author: Ingeborg
6 """
7
8 import glob
9 import numpy as np
10 import spectral.io.envi as envi
11 import matplotlib.pyplot as plt
12
13 """
14 Step 1:
15     Images are loaded and stacked into the list L1.
16     Header data is exdrcted.
17     ROI and WR is located
18 """
19 hdrlist = glob.glob('*.hdr')
20 filelist = glob.glob('*.hyspex')
21 L1 = np.array([envi.open(hdrlist[i], filelist[i]).load() for i in
22                 range(len(hdrlist))])
23
24
25 headerfile_swir = open(hdrlist[0], 'r')
26 hdr_swir = headerfile_swir.read()
27 for i in range(len(hdr_swir)):
28     if hdr_swir[i:i+5] == '937.4' or hdr_swir[i:i+6] == '1695.6':
29         print(i)
30
31
32 wavelength_swir = hdr_swir[707:2642].split(',')
33 for i in range(len(wavelength_swir)):
34     wavelength_swir[i] = float(wavelength_swir[i])
35
36
37 wavelength_scientific = [float('{0}E-9'.format(wavelength_swir[i]))
38                           for i in range(len(wavelength_swir))]
39 h = 6.63E-34
40 c = 3E8
41 eV_hyspex= [(h*c/wavelength_scientific[i])/1.6E-19 for i in
42                 range(len(wavelength_scientific))]
43
44 plt.figure(1)
45 plt.imshow(np.sum(L1[2], axis=2), cmap='jet', clim=(0,2500))
46 plt.colorbar()
47 plt.show()

```

```

48
49 """
50 Step 2:
51     ROI images are stacked in list L2
52 """
53
54 L2 = []
55 for img in L1:
56     L2.append(img[81:127,144:145,:])
57     #Choose coordinates for ROI in img
58
59 WR_1 = []
60 for img in L1:
61     WR_1.append(img[338:510,181:230,:])
62     #Choose coordinates for WR in img
63
64 """
65 Step 3 - 4:
66     Use numpy mean to get the spectral mean of each image
67     ROI mean images are divided by the WR and stacked in L3
68 """
69 L3 = []
70 for img, img_WR in zip(L2, WR_1):
71     L3.append([np.mean(img[:, :, k])
72                /np.mean(img_WR[:, :, k]) for k in range(np.shape(img)[2])])
73
74
75 L4 = []
76
77 for k in range(150):
78     list_i = []
79     for i in L3:
80         list_i.append(i[k])
81     L4.append(np.mean(list_i))
82     #Which is done for OC and SC images
83
84
85 """
86 Step 5:
87     The difference spectra is collected by
88     subtracting SC image from OC image,
89     here L4_OC and L4_SC respectively
90 """
91 difference_spectra = [L4_OC[i] - L4_SC[i] for i in range(len(L4_OC))]

```


Appendix B

Additional results from data analysis of HSI acquired in Experiment 3: Test Case 3

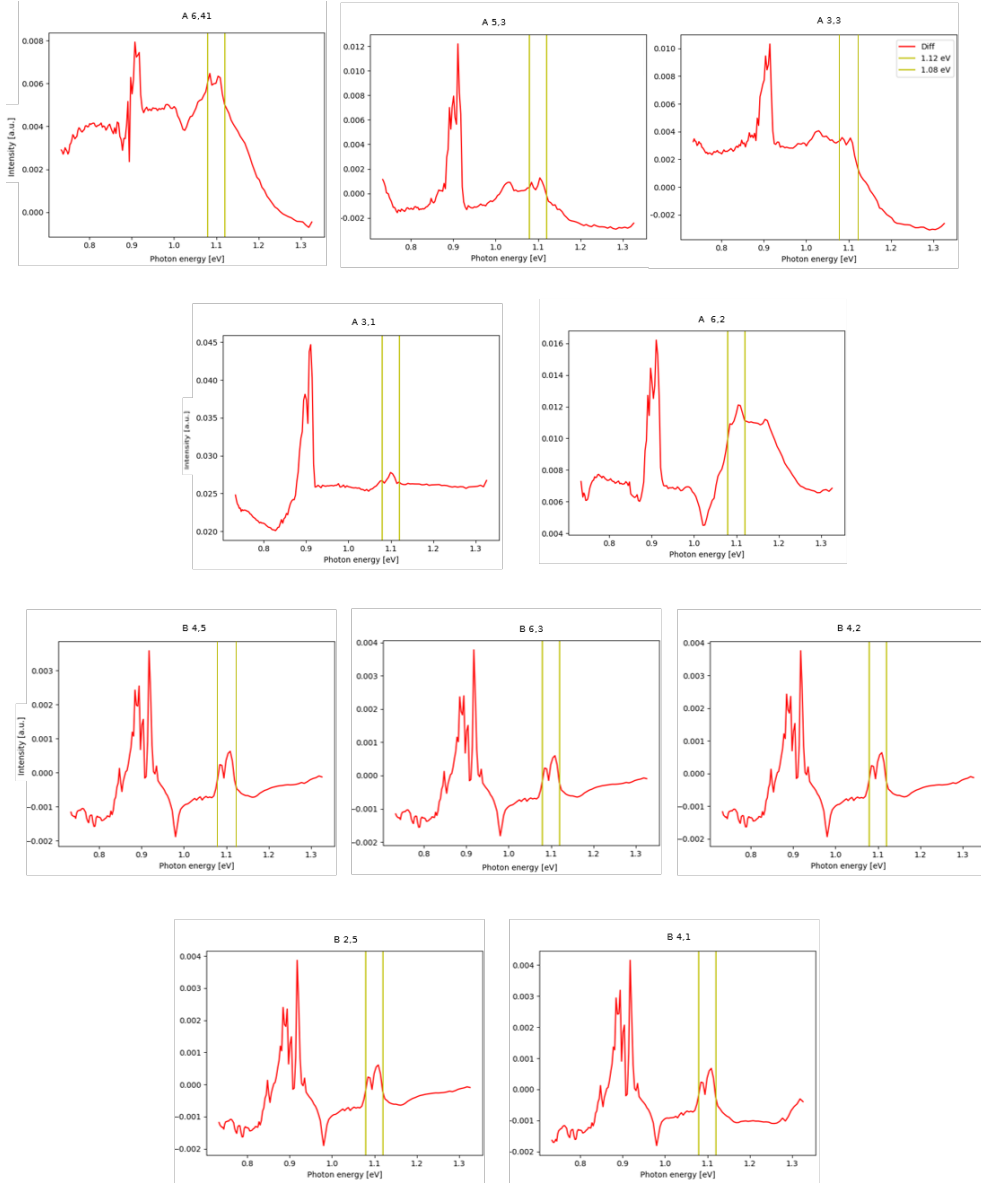


Figure B.1: Spectra of different cells corrected by white reference. The BB signal is expected to lay between the vertical yellow lines. Even though the signal at BB is small, there is an elevation in this area for all cells.

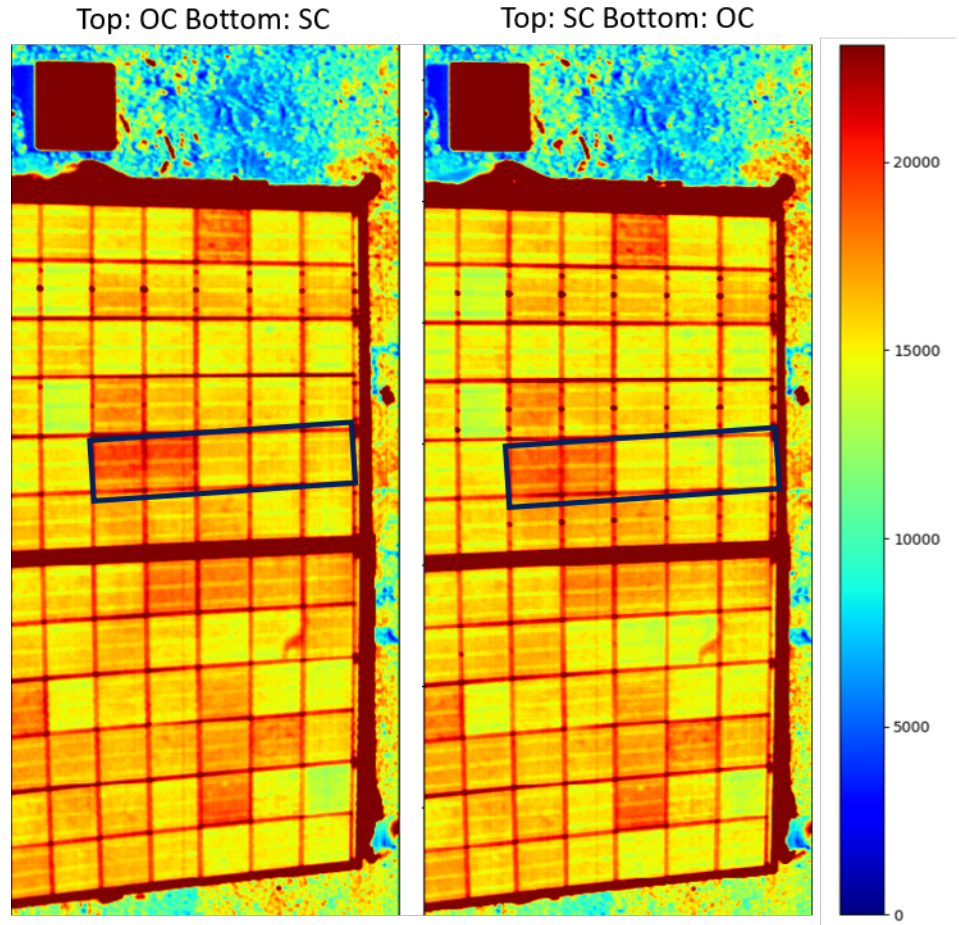


Figure B.2: HSI with colorbar representing signal intensity, integrated over bands 32-42 (100-1151 nm) from experiment 3: test case 3. In the image to the left the top module is in OC and the bottom one is in SC, on the image to the right the top module is in SC and the bottom one in OC. There are not major differences between the two images, but in the cells marked with a dark blue rectangle, one can see a higher signal in the OC image than the SC image. The colorbar represent signal intensity. This support the theoretical assumption that the OC image will display more signal than the SC image, but the difference was expected to be bigger.

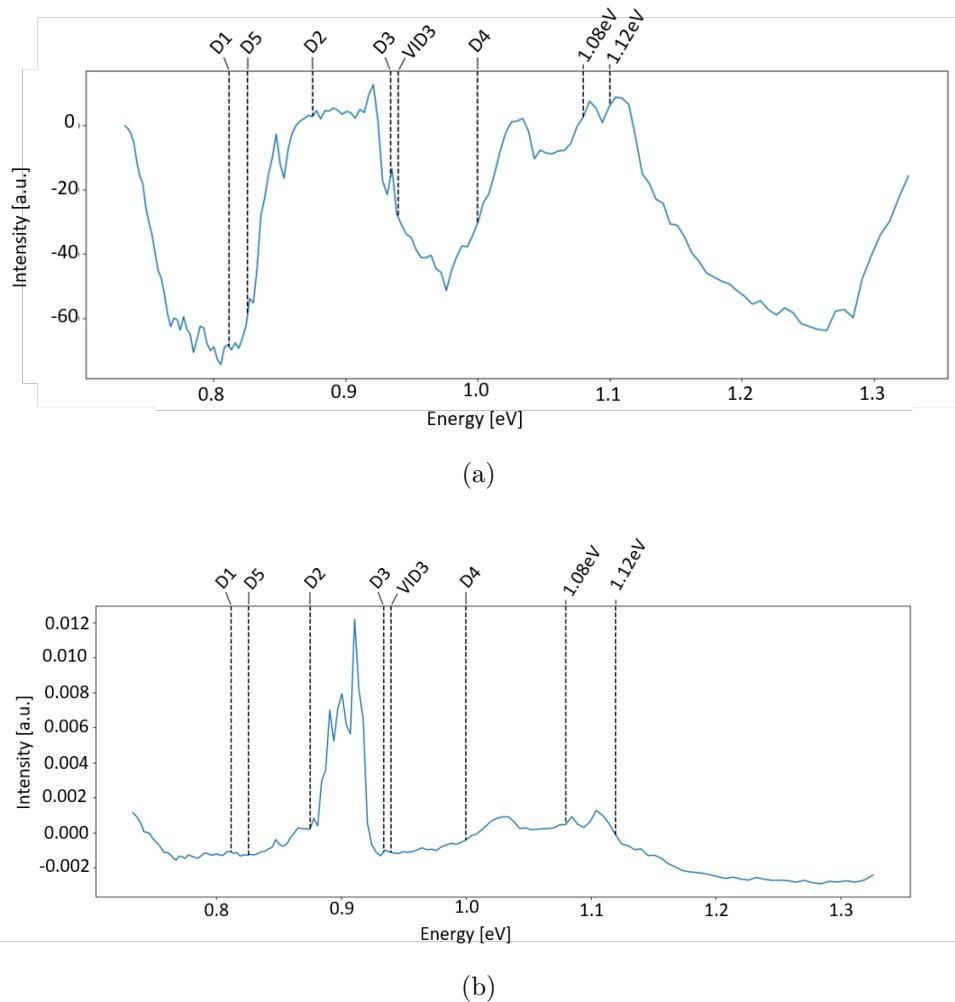
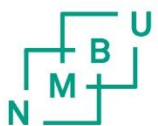


Figure B.3: Spectra of cell A5,3. (a) shows spectra of OC-SC, and (b) shows OC-SC corrected by WR. The vertical lines indicate locations for DRL. These figures show what was assumed from laboratory results in Exp. 1 and 2, that DRL can not be recorded outdoor.



Norges miljø- og biovitenskapelige universitet
Noregs miljø- og biovitenskapslelege universitet
Norwegian University of Life Sciences

Postboks 5003
NO-1432 Ås
Norway